

JGR Solid Earth

RESEARCH ARTICLE

10.1029/2021JB023026

Key Points:

- We use a template matching method to rebuild an earthquake catalog for Taiwan 7 months before and 12 months after 2009 typhoon Morakot
- The seismicity rate of a 40-day earthquake sequence in northeastern Taiwan was reduced significantly after the passage of Morakot
- The seismicity rate increased slightly but without clear *b*-value change after Morakot in typhoon-driven landslide zone in southern Taiwan

Supporting Information:

Supporting Information may be found in the online version of this article.

Correspondence to:

Q. Zhai,
qszhai@gatech.edu

Citation:

Zhai, Q., Peng, Z., Chuang, L. Y., Wu, Y.-M., Hsu, Y.-J., & Wdowski, S. (2021). Investigating the impacts of a wet typhoon on microseismicity: A case study of the 2009 typhoon Morakot in Taiwan based on a template matching catalog. *Journal of Geophysical Research: Solid Earth*, 126, e2021JB023026. <https://doi.org/10.1029/2021JB023026>

Received 13 AUG 2021

Accepted 5 DEC 2021

Author Contributions:

Conceptualization: Zhigang Peng, Shimon Wdowski

Data curation: Lindsay Y. Chuang, Yih-Min Wu

Formal analysis: Qiushi Zhai

Funding acquisition: Zhigang Peng, Shimon Wdowski

Methodology: Qiushi Zhai, Zhigang Peng, Yih-Min Wu

Resources: Zhigang Peng, Yih-Min Wu



Supervision: Zhigang Peng, Shimon Wdowski

Validation: Qiushi Zhai, Ya-Ju Hsu

Writing – original draft: Qiushi Zhai, Zhigang Peng, Ya-Ju Hsu

Writing – review & editing: Qiushi Zhai, Zhigang Peng, Lindsay Y. Chuang,

Investigating the Impacts of a Wet Typhoon on Microseismicity: A Case Study of the 2009 Typhoon Morakot in Taiwan Based on a Template Matching Catalog

Qiushi Zhai¹ , Zhigang Peng¹ , Lindsay Y. Chuang¹, Yih-Min Wu^{2,3} , Ya-Ju Hsu^{2,3} , and Shimon Wdowski⁴ 

¹School of Earth and Atmospheric Sciences, Georgia Institute of Technology, Atlanta, GA, USA, ²Department of Geosciences, National Taiwan University, Taipei, Taiwan, ³Institute of Earth Sciences, Academia Sinica, Taipei, Taiwan, ⁴Department of Earth and Environment, Institute of Environment, Florida International University, Miami, FL, USA

Abstract Recent studies suggested that transient and long-term stress changes caused by Earth's surface processes (e.g., extreme weather events, annual variations on groundwater storages) can affect earthquake activities in the subsurface. However, these studies may be limited by the completeness of standard earthquake catalogs, especially during or right after extreme weather events. Here we apply the template matching method to build a more complete earthquake catalog in Taiwan spanning seven months before and 12 months after 2009 typhoon Morakot, which brought the highest rainfall in southern Taiwan in the past 60 years and triggered numerous landslides. We then use the enhanced catalog to investigate possible influences of typhoon-driven Earth's surface processes (atmospheric pressure, precipitation, and erosion) on local seismicity. We find that the seismicity rate of a 40-day earthquake sequence in northeastern Taiwan was reduced significantly right after the passage of typhoon Morakot's eye center. In the typhoon-triggered landslide zone in southern Taiwan, we find a slight increase in background seismicity rate in the next year after Morakot, matching the results of a recent study. However, we do not observe a clear change in the Gutenberg-Richter *b*-value in this zone, which is different from the recent study. Station outages during and right after Morakot prevents us from better understanding short-term precipitation effect on local seismicity. Overall, except for a reduction in seismicity rate near the typhoon's low-pressure eye center in northeastern Taiwan, we do not observe other clear seismicity changes that can be attributed to surface changes induced by typhoon Morakot.

Plain Language Summary It is important to study cascading nature hazards (typhoons/hurricanes, landslides, earthquakes, etc.) because of their threats to human life and property. 2009 typhoon Morakot is the deadliest typhoon in Taiwan, which brought the highest rainfall in the past 60 years and led to numerous landslides. To investigate the possible influences of Morakot on subsurface earthquake activities, we build a more complete earthquake catalog for Taiwan spanning seven months before and 12 months after 2009 typhoon Morakot. This enhanced earthquake catalog includes many small earthquakes that cannot be felt by local residents in their ordinary life and were not in the standard earthquake catalog. In northeastern Taiwan, our results show that a 40-day earthquake sequence was apparently shut down right after the passage of typhoon Morakot. If this observation is not a pure coincidence, it may suggest that the low-pressure system of typhoon Morakot was capable of modulating the subsurface seismicity behavior. In southern Taiwan, the heavy-rainfall and landslide region, we do not observe clear seismicity changes that can be attributed to surface changes induced by typhoon Morakot.

1. Introduction

Earthquakes occur in the subsurface but can also alter the Earth's surface. Examples include surface ruptures (Bonnilla et al., 1984; Peltzer et al., 1998; Wesnousky, 2008), and shaking-induced landslides (Keefer, 2002; Khazai & Sitar, 2004; Rodriguez et al., 1999; Yin et al., 2009). However, the influence of Earth's surface processes on subsurface fault slip and earthquake behaviors remains poorly understood. Previous observational and modeling studies have shown that certain surface processes are capable of generating loading/unloading stresses and modulating earthquake behaviors. These include variations in atmospheric pressures (Gao et al., 2000; Hsu et al., 2015; J. W. Lin, 2013; Liu et al., 2009; X. F. Meng et al., 2018), reservoir impoundment and fluctuations in reservoir water level (Lei, 2011; McGarr et al., 2002; Tao et al., 2015), construction (C. H. Lin, 2005; Qian et al., 2019),

Yih-Min Wu, Ya-Ju Hsu, Shimon Wdowinski

seasonal water storage and snow load/unload (Bettinelli et al., 2008; Heki, 2001, 2003; Hsu et al., 2021; Johnson et al., 2017a, 2017b, 2020), glacier load and unload (Grollimund & Zoback, 2001; Thorson, 1996; Wu & Johnston, 2000), erosion and sedimentation (Calais et al., 2010; Jeandet Ribes et al., 2020; Maniatis et al., 2009; Steer et al., 2014, 2020), and pore pressure changes due to rainfall and other extreme weather events (Costain & Bollinger, 2010; Hainzl et al., 2006; Husen et al., 2007; Kraft et al., 2006; Miller, 2008; Roth et al., 1992).

The time scales of these surface variations and the associated stress perturbations are broad, ranging from hours (e.g., extreme weather events), days to years (e.g., annual variations in water cycles), to hundreds to million years (e.g., long-term erosion). The stress perturbations range from a few kilopascals (KPa) (Gao et al., 2000) to a few megapascals (MPa) (Manga & Brodsky, 2006; Steer et al., 2014). While results from some studies were later confirmed by subsequent works (e.g., Hainzl et al., 2006, 2013; Kraft et al., 2006; Svejdar et al., 2011), there are still many open questions on the robustness of some observations and the underlying physical mechanisms. For example, Liu et al. (2009) interpreted the transient strain observed in borehole strainmeters located in eastern Taiwan as evidence for typhoon-triggered slow earthquakes. However, Hsu et al. (2015) found that the same observed strain changes are mostly associated with environmental factors such as rainfalls, rather than subsurface slip from slow earthquakes. Mouyen et al. (2017) strengthened the findings of Hsu et al. (2015) by quantifying the contributions of air pressure, ocean loading and rainfalls on surface deformation. While stress changes from long-term surface processes (e.g., seasonal water storage and snow load) generally show robust correlations with seismicity (e.g., Hsu et al., 2021; Johnson et al., 2017b), it is still not clear whether transient stress changes from short-term events (e.g., tropical cyclones) are capable of triggering earthquake activities (X. F. Meng et al., 2018; Steer et al., 2020).

An ideal region to examine the relationship between short-term surface processes and subsurface seismic activity is Taiwan (Figure 1). Located at the boundary between the Eurasian and the Philippine Sea plates, Taiwan is seismically active (Tsai, 1986) and is monitored by dense and permanent seismic networks (Shin, 1992). In addition, Taiwan frequently experiences tropical cyclones (also known as typhoons in Northwest Pacific, or hurricanes in Atlantic or Northeast Pacific). Typhoons can cause significant short-term changes such as atmospheric pressure variations (Chen, 2009) and extreme precipitation (Chien & Kuo, 2011), trigger landslides (C.-W. Lin et al., 2011), and facilitate long-term erosional processes (Dadson et al., 2003). Based on historical records of these atmospheric, hydrological, and geological phenomena, Lin (2013) studied 102 typhoons that traversed or passed nearby Taiwan from 1995 to 2011 and found a 63.75% earthquake-triggering probability by a typhoon. Among them, the 2009 typhoon Morakot produced the highest rainfall in southern Taiwan in the recent 60 years (Chien & Kuo, 2011). Morakot made landfall in Taiwan on 8 August 2009 (Figure 1), delivered up to 3 m of rainfall in five days between August 6 and 10, 2009 (Chen, 2009; Chien & Kuo, 2011), and led to more than 20,000 landslides and subsequent erosional processes in Southern Taiwan (Hung et al., 2018; C. H. Lin et al., 2015; C.-W. Lin et al., 2011; Steer et al., 2020). Therefore, we select the 19-month period around typhoon Morakot in Taiwan as the target time window of our study.

In a recent study, Steer et al. (2020) found possible changes in earthquake statistics at 0–15 km depth in southern Taiwan following typhoon Morakot. They concluded that these changes were induced by landslides and subsequent erosion driven by typhoon Morakot and lasted for at least 2.5 years. In another recent study, Hsu et al. (2021) found seasonal seismicity rate variations in western Taiwan. They proposed that these variations are driven by interannual hydrological changes in that region. Both studies utilized earthquakes listed in the Central Weather Bureau Seismic Network (CWBSN) catalog. However, standard catalogs are inherently incomplete, especially in the lower magnitude ranges, or right following large earthquakes with high background noises and overlapping arrivals (Chang et al., 2007; Enescu et al., 2007; Kagan, 2004; Peng et al., 2006). Because extreme winds and heavy rainfalls are generally associated with wet typhoons and can generate high seismic noises, we expect that the CWBSN catalog may not be complete, at least in the time windows during and right after typhoon Morakot.

In this study, we first build a more complete earthquake catalog for Taiwan from 7 months before to 12 months after typhoon Morakot. We use a matched filter technique (MFT, also known as template matching) (Gibbons & Ringdal, 2006; Peng & Zhao, 2009; Shelly et al., 2007) to detect possible small earthquakes that are not listed in the CWBSN catalog. We also relocate the detected events based on waveform-correlated differential times, and determine their focal mechanisms based on first-motion polarities from a deep-learning model. Finally, we use

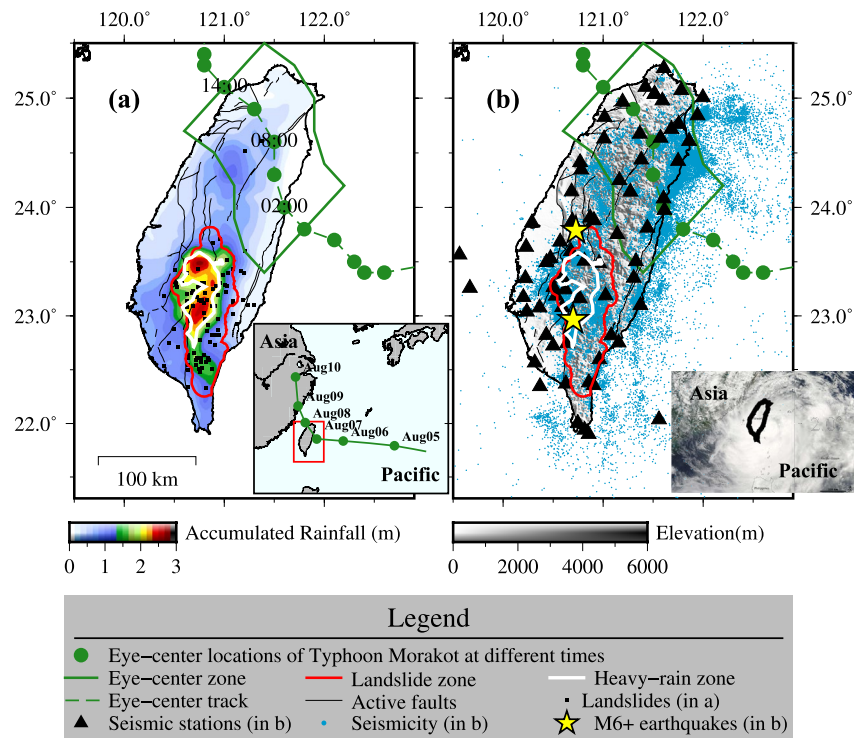


Figure 1. Typhoon Morakot and seismic network in Taiwan. (a) Typhoon-induced accumulated rainfall and landslides. The rainfall/precipitation data of 5 days (6–10 August 2009) are from Central Weather Bureau. The green dots on the green dashed line are the eye-center locations at different times on 8 August 2009 (GMT+8). The green line marks the zone within ~60 km of the eye-center locations of Morakot, termed the eye-center zone in this study. The black squares are Morakot-induced landslides listed in C. H. Lin et al. (2015). The red line marks the zone with a high spatial density of landslides triggered by typhoon Morakot. This zone is the same as in Steer et al. (2020), termed the landslide zone in this study. The white line is the 2-meter contour of the accumulated rainfall, termed the heavy-rain zone in this study. The black lines are active faults. In inset marks the study region (red box) and the typhoon path (green line) in a larger map of the Asia-Pacific. The blue dots mark the locations at 8 PM on these days. (b) Seismic stations of Central Weather Bureau Seismic Network (CWBSN) and seismicity in the Wu catalog (Wu, Chang, et al., 2008) from 1 January 2009 to 31 July 2010. The two yellow stars are two magnitude (M) 6+ earthquakes that occurred 3 and 9 months after typhoon Morakot (North: M6.0 Nantou earthquake on 5 November 2009, at 24-km depth; South: M6.4 Jiashian earthquake on 4 March 2010, at 22-km depth). The colored lines are the same as in (a). The inset shows a satellite image of Morakot on 7 August 2009 (adapted from a NASA image), the black line marks the coast of Taiwan main island.

the updated catalogs to investigate the spatiotemporal properties of seismicity before and after typhoon Morakot and examine possible influences of typhoon Morakot on local seismicity.

2. Data

2.1. Continuous Waveforms and Template Catalog

In this study, we use raw continuous waveforms recorded by CWBSN over the study period from 01/01/2009 to 07/31/2010 in Taiwan (Shin, 1992). CWBSN includes 71 three-component short-period stations with a sampling rate of 100 Hz (Figure 1b). We use as templates 32,802 local earthquakes within our study period and study region (latitude: 21°–26°N, longitude: 119°–124°E) listed in a 3D relocated seismicity catalog (Wu, Chang, et al., 2008), which is termed the Wu catalog in this study. We use the Wu catalog instead of the standard CWBSN catalog that contains 33,496 events, mainly because the Wu catalog has more accurate locations based on a 3D velocity model. The Wu catalog also includes 454,055 *P* wave arrival times, 372,083 *S* wave arrival times, and 42,119 *P* wave first-motion polarities manually determined by CWBSN analysts for the template events used in this study.

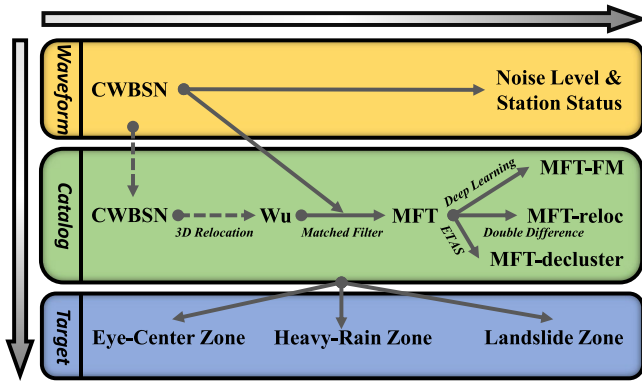


Figure 2. The general workflow of this study. The gray arrows mark the work done in this study and the gray dashed arrows mark the work done in previous studies. The yellow panel summarizes the continuous waveform data used in this study (Section 2). The green panel summarizes the catalogs used/built in this study. "CWBSN" means the CWBSN catalog used in Steer et al. (2020). "Wu" means the 3D relocated seismicity catalog (Wu, Chang, et al., 2008), which is also the catalog of template events used in earthquake detection with matched filter technique (Section 2.1 and 3.1). The "MFT", "MFT-reloc", "MFT-FM", and "MFT-decluster" are the MFT catalogs after detection (Section 3.1), after relocation (Section 3.2), after measuring the focal mechanism (Section 3.3), and after declustering (Section 4.2), respectively. The blue panel shows three different target regions analyzed in this study with the catalogs mentioned above. The location of "Eye-Center Zone" (Section 4.4 and 5.2), "Heavy-Rain Zone" (Section 4.5 and 5.3), and "Landslide Zone" (Section 4.6 and 5.4) can be found in Figure 1.

2.2. The Number of Stations in Operation and Noise Energy Estimation

A seismic station's operational status and noise level can affect its ability to record local microseismicity. Typhoon Morakot brought strong wind and heavy rainfall to Taiwan, which increased seismic noise recorded by the CWBSN stations. In addition, some stations did not work properly during or right after such an extreme weather event due to power and communication outages, and equipment damages. In this section, we measure the daily number of operating stations and daily background noise to better understand how these changing parameters affect the subsequent analysis of seismicity rate changes.

First, we measure the daily number of operational stations. We manually check the raw 24-hour waveforms and evaluate that are no data gaps in the raw waveforms. However, in certain time windows, all data points have exactly the same value (i.e., 0, -1, +1), indicating that the corresponding component of that station was not in fully operational during these time windows. For each 24-hour waveform, we measure the total length of the constant-value windows by counting the total number of points, in which the k^{th} derivative is equal to zero. The result is not sensitive to k , because the k^{th} derivative of a constant-value curve is always zero, regardless of the value of the positive integer k . For simplicity, we set $k = 10$ in this study. Although the tenth derivative requires plenty of data points to calculate, it is needed in order to identify the long constant-value window. Next, we define an operational ratio (o-value) of a given 24-hour waveform by 1 minus the result of the constant-value window length divided by the total length (24 hr). We find that the distribution of o-values of all waveforms we used is clearly bimodal, either close to 0 or close to 1 (Figure S1 in Supporting Information S1). Hence,

we set an o-value of 0.95 as the threshold for an operational station. For each station on each day, we count the station as operational on that day if the o-values of three components are all higher than the threshold.

Next, we use the waveforms of operational stations to measure the average noise energy of each day. The daily average noise energy is defined as:

$$E_{\text{noise}}(d) = \text{mean}_s \left\{ \text{mean}_c \left\{ \text{median}_t [A^2(d, s, c, t)] \right\}_{\text{norm}} \right\} \quad (1)$$

where E_{noise} is the noise energy; A^2 is the squared amplitude of the 2–16 Hz bandpass-filtered waveform at day d , station s , component c , and time t ; $\text{median}_t[\cdot]$ is the median value over time; $\text{mean}_c\{\cdot\}$ is the average value of all components; $\text{mean}_s\{\cdot\}$ is the average value of all stations; and norm is normalization. The 2–16 Hz frequency band of the filter is the same as used in the earthquake detection described in the following section. We take a median value instead of an average value of the waveform amplitude in order to reduce the effect of local transient high-noise outliers. The normalization is applied before averaging to balance the weights of different stations. Figure S2 in Supporting Information S1 shows that the noise level during weekends is clearly lower than during workdays. The noise level during the Spring Festival (also known as Lunar or Chinese New Year) holidays in January 2009 and February 2010 is even lower.

3. Building a New Seismicity Catalog

3.1. Earthquake Detection

To detect possible small earthquakes that are not listed in the CWBSN catalog, we use waveforms of template events to scan through continuous waveforms with the MFT (Peng & Zhao, 2009). We use a GPU-based package developed by X. Meng et al. (2012) to perform this task. Figure 2 shows a general workflow in this study, largely following those used in several recent studies (X. F. Meng et al., 2018; Ross, Trugman, et al., 2019) and is described below.

First, we down-sample all the raw continuous waveforms from 100 to 50 Hz to speed up the subsequent computation. Then, we apply a bandpass filter of 2–16 Hz to these waveforms to enhance signals of local events. Template waveforms of the 32,802 local earthquakes are cut from the filtered continuous waveforms based on the phase arrival times in the Wu catalog. We compute the signal-to-noise ratio (SNR) for all template waveforms. The *P*-wave signal is 3 s or $S-P + 0.5$ s (whichever is shorter) long starting 0.5 s before its arrival time. The *S*-wave signal is 5 s long starting 0.5 s before its arrival time. The noise window is 5 s long ending 0.5 s before the *P* arrival time. To avoid false detections by a few noisy template waveforms, we only select template events having more than 6 waveforms with SNRs greater than 5.

Next, we calculate the stacked cross-correlation (CC) functions for each day of continuous waveforms in our study period and each of these selected template events. To calculate the CC functions for each event-station pair, we use 4 s long windows for both *P*- and *S*-waves starting 0.5 s before their arrival times. All stations within 100 km of the source-receiver distances are used. We only use the vertical component for the *P* wave and horizontal components for the *S* wave. To enhance earthquake signals and suppress uncorrelated background noise, we shift CC functions to the origin time of the template with the corresponding travel times and stack the shifted CC functions. We calculate the median absolute deviation (MAD) for the stacked and normalized CC functions. An initial detection threshold is set at 9 times the MAD (Shelly et al., 2007). After repeating these steps for all continuous waveforms and all selected template events, we obtain an initial list of detected events (detections).

We then use the following steps to refine this initial list of detections. Because a new event could be detected by multiple template events, there are many duplicated events listed in the initial catalog. To remove these duplicated events, we only keep the highest-MAD detection in each group of detections (separated by less than 2 s) and delete the other detections. Next, we measure the local magnitudes (M) of the newly detected events based on the median peak amplitude ratios between the detected and the template events (Peng & Zhao, 2009). We calculate the logarithm of the median peak amplitude ratio and assume that a factor of 1 difference in magnitude is equal to a factor of 10 difference in amplitude. To ensure that the magnitudes of the newly detected events are well-calibrated, we only use peak amplitude ratios of waveform pairs that meet the following two criteria: (a) SNR of the new detected *P*-wave or *S*-wave ≥ 4 ; and (b) maximum CC coefficient ≥ 0.6 . The data window for the CC calculation is 1 s for *P* waves and 1.5 s for *S* waves, starting 0.25 s before the arrival time. We allow 1 s shift for *P* wave and 1.5 s shift for *S* wave, and apply it to the original data with 100 Hz. This is the same window length used later for obtaining differential travel times and relocations described in the next section.

Finally, we use the following procedure to remove events with relatively large magnitudes and relatively low CC values (but above the 9 times MAD threshold). The procedure is based on the expectation that larger earthquakes should be observed on more stations and components with high SNRs. A newly detected event with magnitude M , is kept as long as it has at least n ($n = 3^{(M-1)}$) components that meet the aforementioned two criteria. Otherwise, the event is removed from the catalog. We limit the n as a value between 1 and 15. If the calculated n is not in this range, we set it as 1 or 15 (whichever it is closed to). This is an empirical estimation based on our visual examination of hundreds of detections, and is somewhat similar to threshold values often used in relocation programs such as hypoDD (Waldhauser & Ellsworth, 2000). For example, a magnitude 2 event would require 3 components, a magnitude 3 event would require 9 components, and a magnitude 4 (and above) would require 15 components.

The newly built catalog from MFT detection contains 218,155 earthquakes (Data set S1 in the Supporting Information S1), which is termed the MFT catalog in this study. The number of events in the MFT catalog is a seven-fold increase compared to the Wu catalog (templates). Most of the newly detected earthquakes are below magnitude 2. In the two weeks during and after typhoon Morakot (6–19 August 2009), the number of events in the MFT catalog (2,472) is a four-fold increase compared to the Wu catalog (648). Figure 3 shows an example of a newly detected event on 8 August 2009 (when typhoon Morakot made landfall in Taiwan) and its corresponding template event. The template event is a magnitude 1.88 earthquake that occurred on 2009-08-06T00:29:03.29. The newly detected event is a magnitude 1.90 earthquake that occurred on 2009-08-08T08:15:04.66 (~2 days after the template event). The mean CC value of this detection is 0.53, which is 25.7 times the MAD, suggesting that it occurred close to the template event.

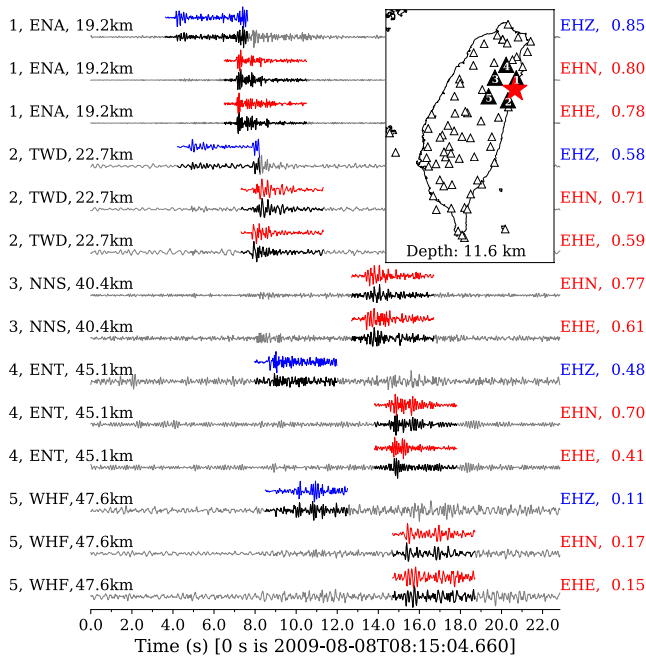


Figure 3. An example of a newly detected event on 8 August 2009 (when typhoon Morakot made landfall in Taiwan) and its corresponding template event. The blue waveforms are the P wave of the template, the red waveforms are the S wave of the template, the gray colors mark the continuous waveforms, and the black sections on the gray waveforms correspond to the newly detected events. The three columns on the left are the station label, station name, and event-station epicentral distance. The two columns on the right are the component name and the CC value on this component. The location of this template (red star) is shown in the inserted map at the upper right corner. All used stations of this detection are marked as filled black triangles in the inserted map. The numbers on these black triangles are the station labels.

3.2. Earthquake Relocation

To improve the location accuracy, we relocate the MFT catalog obtained from the seismicity detection. The MFT catalog contains both template and newly detected events. The template events have been located individually with a 3D velocity model by Wu, Chang, et al. (2008), Wu, Zhao, et al. (2008). Here we first relocate the template events with hypoDD (Waldhauser & Ellsworth, 2000) using just the phase arrival times without the newly detected events. This improves the initial location accuracy of both template and newly detected events for the subsequent relocation process (Ross, Idini, et al., 2019). We next assign the locations, P and S travel times of newly detected events with the same locations and travel times of their best-matching template.

We relocate the MFT catalog with GrowClust, a cluster-based double-difference relocation technique (Trugman & Shearer, 2017). It defines the relative earthquake locations by fitting the observed differential times with a robust L1-norm approach. These precise differential times are measured from waveform cross-correlation (CC). For each earthquake in the MFT catalog, we apply a bandpass filter of 2–16 Hz to the 100 Hz waveforms. The data window for the CC coefficients calculation is 1 s long for P waves and 1.5 s long for S waves, starting 0.25 s before the arrival time. We allow a 1 s shift for the P wave and a 1.5 s shift for the S wave. We then perform the pairwise cross-correlation for each event with up to 1,000 nearest neighbor template events within a 5-km distance. To avoid multiple crustal phases due to regional propagation, we set the maximum source-receiver distance as 100 km. We use a three-point quadratic interpolation to improve the precision of the CC function near its peak value (Shelly, Ellsworth, & Hill, 2016). These differential times and their corresponding waveform similarity (CC) coefficients are the input data for the GrowClust relocation procedure. A local 1D velocity model (Table S2 in Supporting Information S1) averaging from a 3D velocity model of Taiwan (Wu et al., 2007) is used for the relocation.

Our best relocation results are produced by setting the minimum similarity coefficients as 0.6 and the minimum number of differential times as 4 (G. Q. Lin, 2020). To ensure that template events are relocated before newly detected events during the GrowClust inversion process, we increase the similarity (CC) coefficients by a factor of 100 for template-template event pairs, which is the same as in Ross, Trugman, et al. (2019). In the end, 63,587 (30%) earthquakes in the MFT catalog are relocated (Figure 4d). This relocated catalog is termed the MFT-reloc catalog in this study (Data Set S1 in the Supporting Information S1). The number of events in the MFT-reloc catalog is a two-fold increase compared to the standard CWBSN catalog or the Wu catalog.

Figure 5 shows the frequency-magnitude information of our newly built catalogs and the template (Wu) catalog. As expected, most of the newly detected events are in the range of magnitude 2 and smaller. Note that a small number of larger earthquakes are not successfully relocated. This is because larger earthquakes generally have more complex waveforms, so they do not cross-correlate well with other events nearby (G. Q. Lin, 2020; Ross, Trugman, et al., 2019).

In the following sections, we focus primarily on the temporal evolutions of earthquake statistics in the eye-center zone in northeast Taiwan, and the heavy-rain and landslide zones in southern Taiwan (Figure 1). Because the scale of these target zones is about several tens of kilometers, much larger than the subtle location changes between the full MFT and MFT-reloc catalogs, we mostly use the full MFT catalog for subsequent analysis in this study.

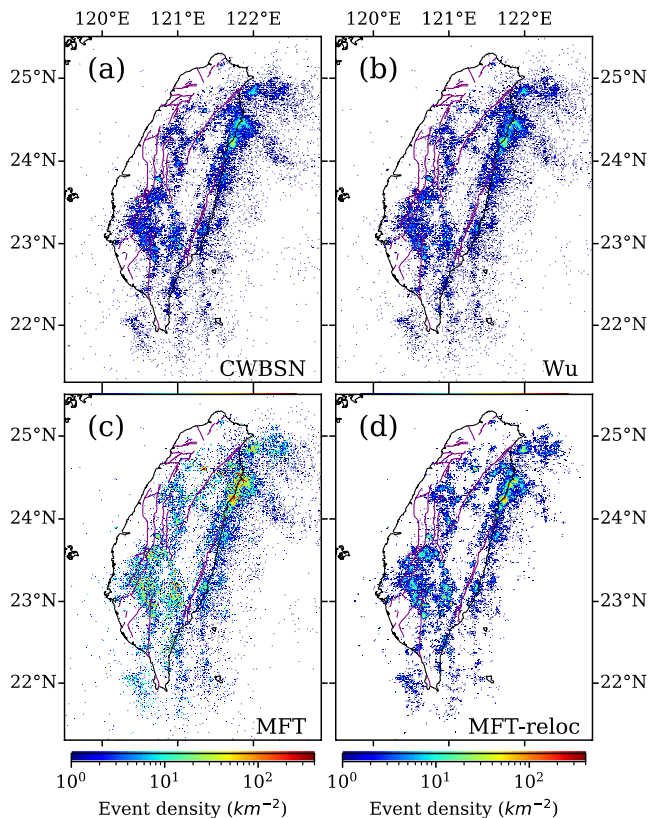


Figure 4. Comparison of earthquake locations listed in the four studied catalogs from 1 January 2009 to 31 July 2010. (a) Earthquake density map of 33,496 events in the Central Weather Bureau Seismic Network catalog. (b) Earthquake density map of 32,802 events in the Wu (templates) catalog. (c) Earthquake density map of 218,155 events in the matched filter technique (MFT) catalog. (d) Earthquake density map of 63,587 events in the MFT-reloc catalog. The purple lines mark active faults in all panels.

3.3. Earthquake Focal Mechanisms

In the Wu catalog, only 548 events have focal mechanism solutions within our space-time windows, which are determined based on the first motions with the GaFpfit package (Wu, Zhao, et al., 2008). In this study, we apply the same package to compute focal mechanism solutions for earthquakes in the MFT catalog using the polarities of *P*-wave first motions picked by a deep learning model. We develop this convolutional-neural-network (CNN) based *P*-wave first-motion polarity (CNN-Polarity) model (Figure 6a), which was added into the open-source Yews package developed by Zhu et al. (2019). Our CNN-Polarity model is similar to those used in several recent studies (Cheng & Ben-Zion, 2020; Hara et al., 2019; Ross et al., 2018; Uchide, 2020). The input of this model is a 300-sample waveform, which is 3 s long with a 100-Hz sampling rate. The outputs of this model are two non-negative confidence scores corresponding to the probabilities of the upward and downward polarities (Figure 6a). The sum of the two output scores is 1.

First, we build data sets to train and test this model. We use all the polarity labels (upward: 18,915; downward: 23,204) manually assigned by CWBSN analysts and listed in the Wu catalog. We randomly split the whole data set into training (80%), validation (10%), and test (10%) data sets. Upward polarities are labeled by 0 and downward polarities are labeled by 1. The waveforms corresponding to these labels are cut 1.5 s before and 1.5 s after their arrival times from the 2–16 Hz band-pass-filtered continuous data. Each 3 s long waveform (300 data points) is normalized by its maximum absolute values. We flip the waveforms upside down to equalize the number of upward and downward polarity data (Uchide, 2020). To reduce the uncertainties in the arrival times picking, we randomly apply 100 times of time-shift within ± 1 s to each waveform. The total number of data is hence augmented 200 times by flipping and time-shifting (Uchide, 2020). Then, we train the model with the augmented training data set. After training, we quantify the performance of the trained model based on precision, recall, and F-1 score (Uchide, 2020; Zhu et al., 2019) with the test data set (not used during the training). All of the precision, recall, and F-1 scores of our trained model on the test data set are greater or equal to 95% (Table 1).

Next, we deploy the trained model to the MFT data set. We prepare the waveforms for the MFT data set using the same preprocess as the training data set, but without flipping and time-shifting. We adopt a confidence threshold of 0.7, which is the same as it in Uchide (2020). For a quality control purpose, we require a minimum SNR of 5 for any waveform before picking its polarity. We group all the events detected by the same template event as a family (Chamberlain et al., 2017). We assume that these similar events in a family share a common focal mechanism solution with a first-order approximation (Shelly, Hardebeck, et al., 2016). After deploying the trained model to the MFT data set, we obtain 158,320 predicted *P*-wave first-motion polarities (upward: 63,738; downward: 94,582) for these families. This number of polarities is a four-fold increase compared to it manually assigned by CWBSN analysts and listed in the Wu catalog.

In the end, we use these predicted polarities to calculate the focal mechanisms with the GaFpfit package (Wu, Zhao, et al., 2008). The minimum number of required polarities is 8 (Ross et al., 2018; Uchide, 2020), and the maximum of the stations' coverage gap is 180° (Wu, Zhao, et al., 2008). We obtain focal mechanism solutions of 1,166 families (Figure 6c) corresponding to 3,816 events. This focal mechanism catalog is termed the MFT-FM catalog in this study (Data Set S1 in Supporting Information S1). This number of events in the MFT-FM catalog is a seven-fold increase compared to it (548 events, see Figure 6b) in the Wu catalog (Wu et al., 2010; Wu, Zhao et al., 2008) in our study period and region.

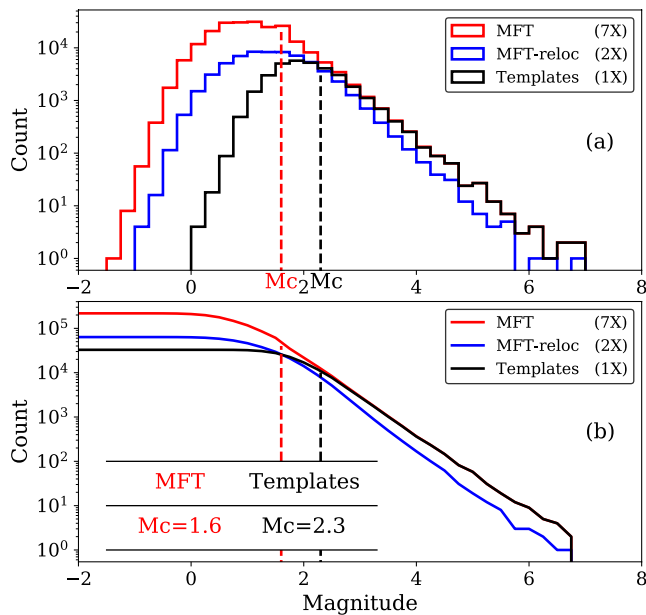


Figure 5. (a) Frequency-magnitude distribution of seismic events listed in the full detection catalog (MFT), the relocated subset of the MFT catalog (MFT-reloc), and the Wu catalog (Templates). (b) The corresponding cumulative frequency-magnitude distribution of these catalogs. The estimated magnitude of completeness (M_c) of the MFT catalog and the Wu catalog (Templates) are 1.6 and 2.3, respectively.

4. Statistics Analysis of the Newly Built Catalogs

4.1. M_c and b -Value Calculation

The magnitude of completeness (M_c) and the parameter b in the Gutenberg–Richter frequency-magnitude relationship (i.e., the G-R law (Gutenberg & Richter, 1944)) are commonly used to characterize statistical behaviors of an earthquake catalog. M_c is the minimum magnitude above which all earthquakes in a given space and time window are reliably recorded. The G-R law is defined as $N(\geq M) = 10^{a-bM}$, which describes the power-law relationship between the magnitude (M) and the total number (N) of earthquakes of at least that magnitude in a given space and time window (Gutenberg, 1956). We use a modified version of the maximum curvature method (MAXC) to calculate the M_c of a given catalog (Wiemer & Wyss, 2000). Specifically, M_c is set to 0.5 plus the maximum of the first derivative of the discrete G-R law plot (Figure 5b), which is the same as in Steer et al. (2020) for direct comparisons in later sections. Note the maximum of the first derivative in Figure 5b is the same as the maximum in Figure 5a. Then, we use all the events above M_c to compute the b -value and its uncertainty with the maximum likelihood estimate method (Aki, 1965). Based on our calculation, the M_c of the full MFT catalog and the Wu catalog (Templates) are 1.6 and 2.3, respectively (Figure 5b). The M_c and b -value of the MFT-reloc catalog are not measured because some large earthquakes are not relocated. To obtain the b -value map, we use spatial sliding windows to further divide and sample the catalogs (Wiemer & Wyss, 2002). The radius of the sliding spatial window is set as 30 km. The minimum number of events with magnitude large or equal to M_c for the calculation of the b -value is set at 50. The sliding-window method and the two parameters are the same as in Steer et al. (2020) for direct comparisons in later sections.

4.2. Declustering the Seismicity Catalog

Microseismicity generally include background (i.e., driven by tectonic or external processes) and clustered (i.e., triggered by previous earthquakes) activity (Gardner & Knopoff, 1974; Zaliapin & Ben-Zion, 2021). In a typical mainshock-aftershocks cluster, aftershocks are triggered by the mainshock, and hence are not considered as independent events. To avoid over-counting these clustered/dependent events, we decluster the MFT catalog, similar to the recent studies in Taiwan (Hsu et al., 2021; Steer et al., 2020). Specifically, we calculate the probability of background seismicity for each event above M_c in the MFT catalog using a stochastic declustering method (Zhuang, 2006; Zhuang et al., 2002, 2004) based on the epidemic-type aftershock sequence (ETAS) model (Table S3 in Supporting Information S1) (Ogata, 1988). For any given space-time window, we calculate "the number of the background seismicity" in this window by summarizing the background seismicity probability of all events above M_c in this window (Meng & Peng, 2014; Zhuang et al., 2005). The number of the background seismicity is then used in the analysis of the seismicity rate around typhoon Morakot. Figures 7 and 8b show the cumulative numbers and the daily numbers (seismicity rate) of the seismicity (above M_c) in the MFT catalog and the background seismicity in MFT-decluster catalog, respectively. As expected, the temporal clustering of seismicity due to moderate-size earthquakes in the MFT-decluster catalog is largely removed. However, it is relatively difficult to observe any clear changes in seismicity associated with typhoon Morakot in a cumulative plot for the entire space-time window (Figure 7). Hence, in the following sections, we focus on different space-time windows and examine the seismicity rates separately.

4.3. General Patterns of Seismicity Rate, Noise Energy, and Station Status

Based on the earthquake detection results (Figure 8) within our study space-time window, we observe a drop in the seismicity rate during and right after typhoon Morakot (Figure 8b). This seismicity-rate drop corresponds to the gap with a triangle shape between magnitude -0.5 and 1 during and right after typhoon Morakot (Figure 8a).

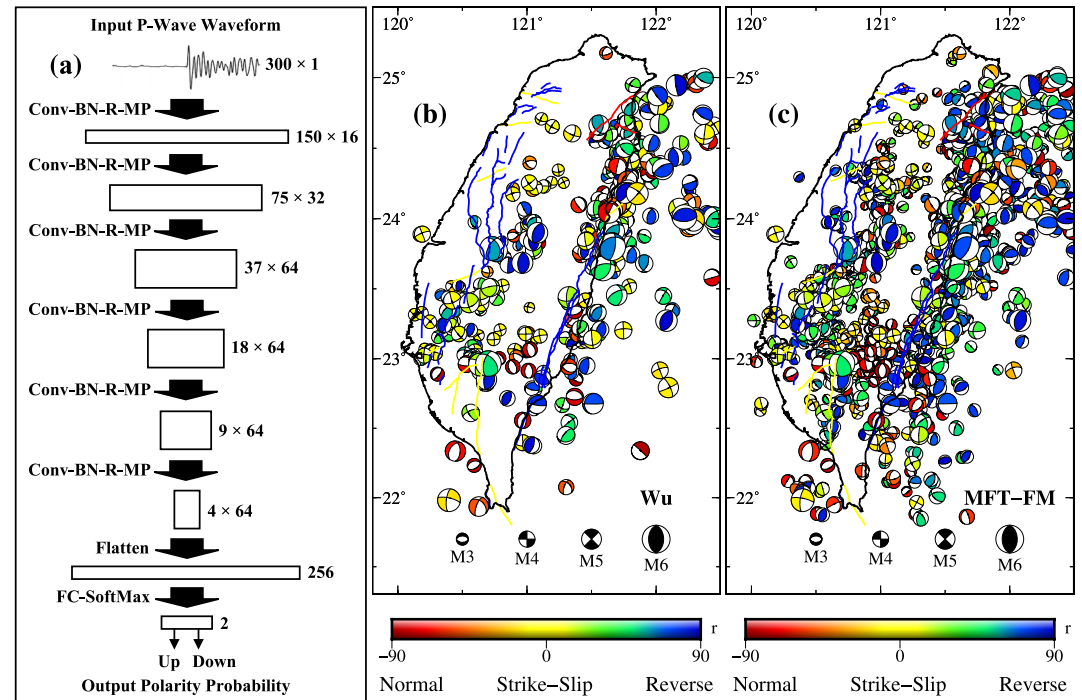


Figure 6. The measurement of focal mechanism solutions with a deep-learning model for polarity picking. (a) A schematic diagram of the convolutional-neural-network (CNN) based P -wave first-motion polarity (CNN-Polarity) model used in this study. The numbers on the right denote the size of samples and channels. There are 6 convolutional layers for feature extraction. The final layer is a fully connected layer for classification. ‘Conv’, ‘BN’, ‘R’, ‘MP’, and ‘FC’ on the left represent convolution, batch normalization, ReLu, max pooling, and fully connected layers, respectively. (b) Map of focal mechanism solutions in the Wu catalog (Wu et al., 2010; Wu, Zhao et al., 2008) in our study period. The focal mechanisms beach balls are color-coded based on the r -value, which is a function of the rake. It can be used to determine the faulting types of earthquakes (Shearer et al., 2006). (c) Map of focal mechanism solutions in the MFT-FM catalog built in this study. Each beach ball denotes the focal mechanism of the template event in each family. The colored lines in b and c mark the active faults in Taiwan (Shyu et al., 2016). Red lines are normal faults. Yellow lines are strike-slip faults. Blue lines are reverse faults.

Our results show the number of operational stations reduced from ~ 70 to ~ 45 right after typhoon Morakot and lasted for 2–3 weeks then recovered to normal (Figure 8c, black bars). We also find that normalized daily average noise energy during several days of typhoon Morakot increased by about two as compared with other days (Figure 8c, reversed red bars).

4.4. Seismicity Near the Eye Center of Morakot in Days Before and After Morakot

Next, we analyze seismicity rate changes near Morakot's eye-center track to examine possible influences of atmospheric pressures on earthquake activities. It took about 12 hr between the landing of Morakot on Taiwan's east coast and its leaving on Taiwan's west coast (Figure 1a). Here we focus on the changes in the seismicity patterns within one week around typhoon Morakot (Figure 9). Figures 9b–9h shows the daily seismicity density maps from 3 days before to 3 days after typhoon Morakot, respectively. Comparing with the seismicity density maps of other days, we do not observe any clear increase on the day that Morakot made landfall on Taiwan island (8 August 2009). However, we do find a small zone (the red box in Figures 9a–9h) with high seismicity density at depth of 0–15 km on northeastern Taiwan near Morakot's eye-center track during these days. The daily seismicity number in this zone decreased with the arrival of typhoon Morakot. As expected, the atmospheric pressure recorded by the HUALIAN-CWB weather station (orange square in Figure 9a, inside the small zone) is lower than normal when the eye center of typhoon

Table 1
Precision, Recall, and F-1 Score of the Two Classification Categories

Categories	Precision	Recall	F-1 score
Upward (0)	0.9563	0.9451	0.9507
Downward (1)	0.9457	0.9569	0.9513

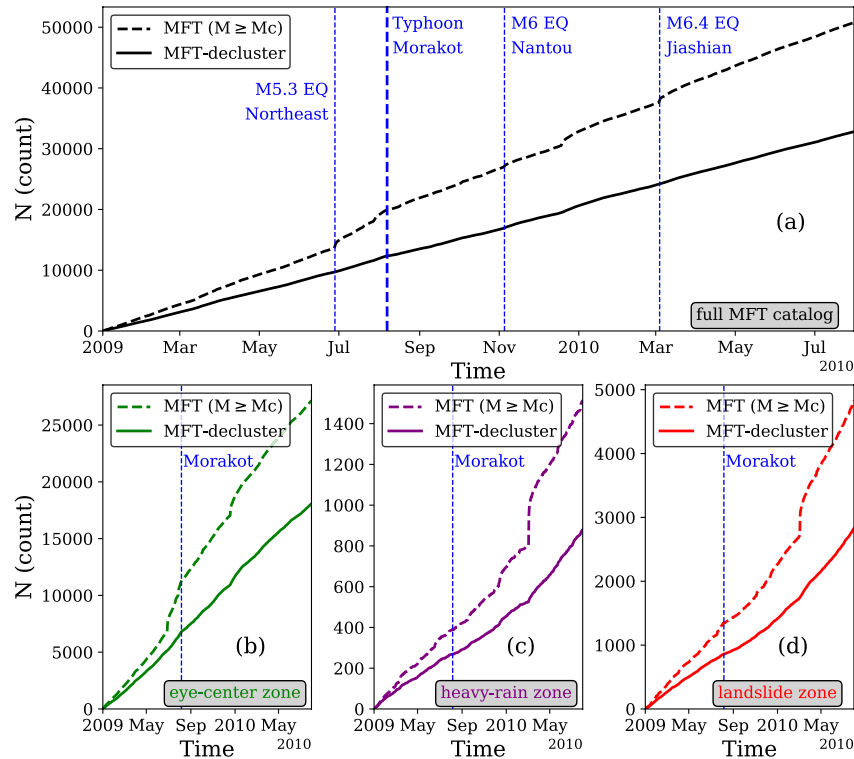


Figure 7. The cumulative number of seismicity (above M_c) in the matched filter technique (MFT) catalog and the background seismicity in MFT-decluster catalog. (a) Events in the full MFT catalog. The vertical blue dashed lines mark a magnitude (M) 5.3 earthquake that occurred in Northeastern Taiwan (will be mentioned in Section 4.4), the typhoon Morakot, the magnitude (M) 6.0 Nantou earthquake (Figure 1b), and the magnitude (M) 6.4 Jiashian earthquake (Figure 1b). (b) Events in the eye-center zone in northeastern Taiwan. (c) Events in the heavy-rain zone in southern Taiwan. (d) Events in the landslide zone in southern Taiwan. The definition and map of these zones can be found in Figure 1.

Morakot passed by (Figures 9i and 9j). The space-time plots of seismicity in this region (Figures 9k and 9l) shows a northward migration of the sequence, which were apparently stopped at the time of typhoon Morakot's landfall.

To examine this further, we check the seismicity in this zone within the 19-month study period (Figure 10). An earthquake sequence starting 40 days before suddenly stopped at the time of typhoon Morakot's passage. Such reduction of seismicity is shown clearly in both the full MFT catalog and the declustered catalog (Figure 10a). This earthquake sequence includes one M5.3 reverse-faulting earthquake that occurred at 12.9-km depth on 28 June 2009 (marked by the star and beachball in Figure 9a) and several M4 earthquakes (Figure 10b). A closer look reveals that the seismicity reduction started the last day before the typhoon landfall on 7 August 2009, when the atmospheric pressure inside this zone is the lowest (Figures 1a and 9j). Most of the earthquakes in this zone are reverse-faulting events (Figure 10c).

To quantify the changing in seismicity rate, we use both β -value statistic and Z-value statistic (Haber-mann, 1981, 1983; Matthews & Reasenberg, 1988; Pankow & Kilb, 2020). β -value statistics is most commonly used in studies of dynamic earthquake triggering (Hill & Prejean, 2015). It measures the difference in seismic rate between a pre-window and a post-window. Therefore, it can be used to evaluate the seismicity rate changes. The β -value is defined as:

$$\beta = \frac{N_{\text{post}} - N_{\text{pre}} * (T_{\text{post}}/T_{\text{pre}})}{\sqrt{N_{\text{pre}} * (T_{\text{post}}/T_{\text{pre}})}} \quad (2)$$

where T_{pre} and T_{post} are the lengths of time windows for counting the number of events before (N_{pre}) and after (N_{post}) the time of interest, respectively. Z-value is an alternative statistical parameter to measure the seismicity rate changes and is a more symmetric version of the β -statistic. We use it as an alternative parameter in this study. The Z-value is defined as:

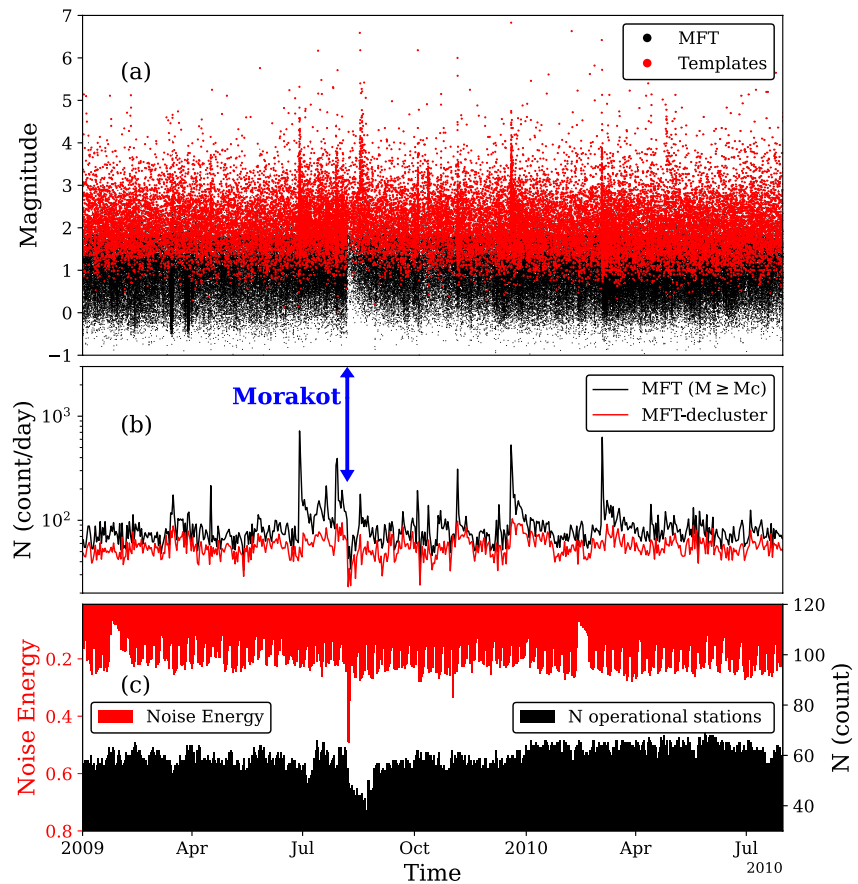


Figure 8. The magnitude-time distribution, seismicity rate, noise energy, and the number of operational stations in this study. (a) Magnitude-time distribution of earthquakes in Wu catalog (templates) and our matched filter technique (MFT) catalog. (b) The seismicity rate (above M_c) of the MFT catalog and the background seismicity rate of the MFT-decluster catalog. The blue arrows mark the day typhoon Morakot landed in Taiwan (8 August 2009). (c) The daily average noise energy (reversed red vertical axis on the left) and the number of operational stations (see the definition in Section 2.2) of each day (black vertical axis on the right).

$$Z = \frac{N_{\text{post}} * T_{\text{pre}} - N_{\text{pre}} * T_{\text{post}}}{\sqrt{N_{\text{post}} * T_{\text{pre}}^2 - N_{\text{pre}} * T_{\text{post}}^2}} \quad (3)$$

where T_{pre} , T_{post} , N_{pre} , and N_{post} are defined as above. We set the window before typhoon Morakot (7 August 2009) starting from the day of the M5.3 earthquake (28 June 2009). We set the window after typhoon Morakot ending on 15 August 2009 (Figure 10b). Then, we use the events at depth of 0–15 km above M_c in the MFT catalog to calculate the β -value and Z-value. We obtain a β -value of -20.45 and a Z-value of -31.42 . The absolute values of both numbers are much higher than the standard significance thresholds of around 2 (Habermann, 1981; Pankow & Kilb, 2020; Reasenberg & Simpson, 1992), even considering that the threshold might vary for different times and regions (Pankow & Kilb, 2020; Prejean & Hill, 2018).

As mentioned before, some seismic stations could work well before typhoon Morakot but went down during or right after Morakot due to power and communication outages, and equipment damages. This may produce a sudden drop in detected seismicity. To rule out this effect, we also present detection results (Figure 10a) that are based solely on the stations (blue triangles in Figure 9a) that were in operation at least 95% of days from ~ 1.5 months before to ~ 1.5 months after typhoon Morakot (1 July 2009–30 September 2009). Although we have smaller numbers of detected events, the general patterns are similar to those based on using all available stations.

It is well known that the aftershock seismicity rate decays with time. The decay law of aftershock activity follows the Omori formula $n(t) = K(t + c)^{-1}$ or its modified form $n(t) = K(t + c)^{-p}$ (Utsu et al., 1995). To rule out the

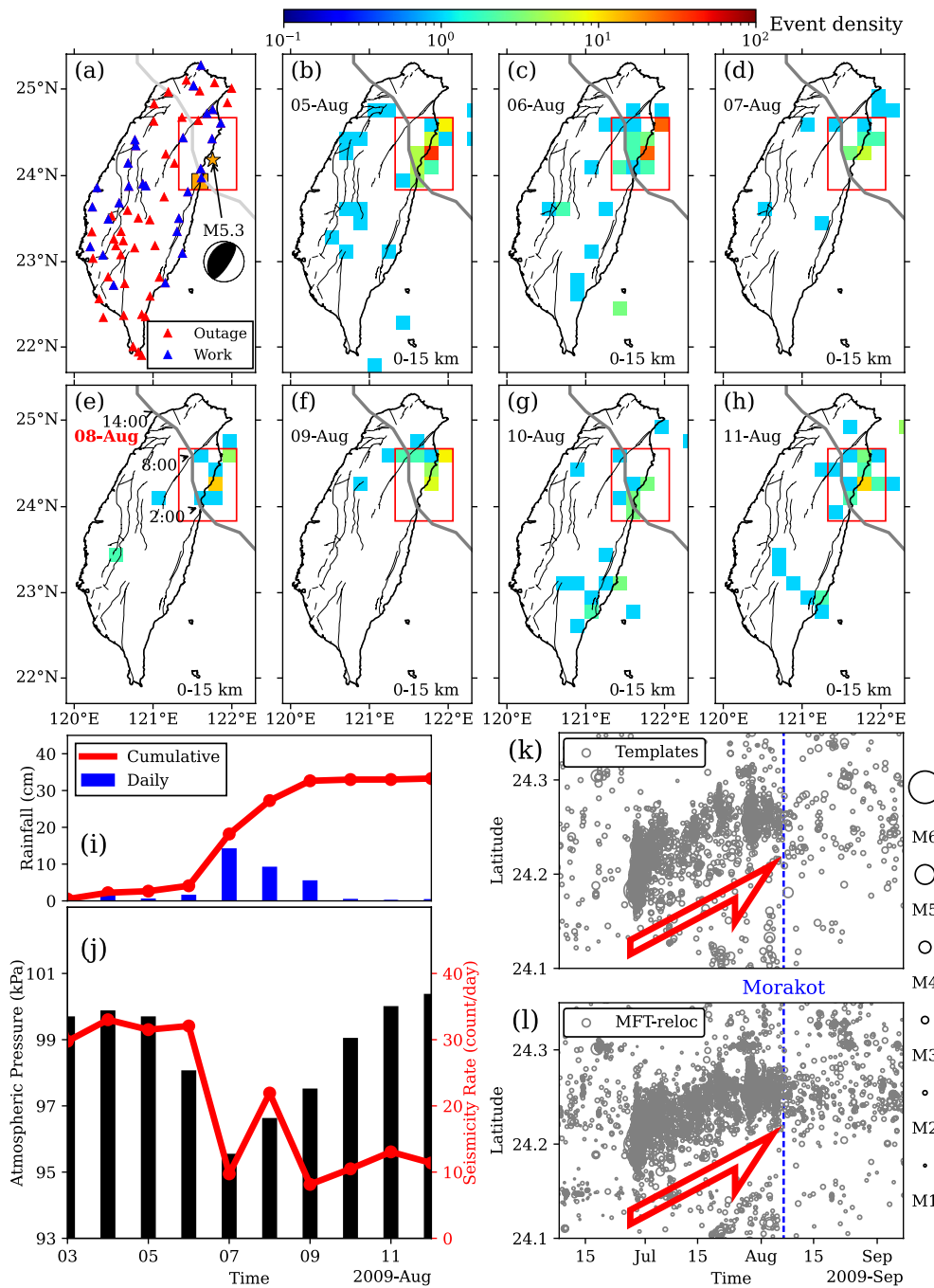


Figure 9. Seismicity in northeastern Taiwan around the time of typhoon Morakot. (a) Station map showing 71 CWB stations used in this study. The blue triangles are stations that were operating (see the definition in Section 2.2) on 95% of days between 1 July 2009 and 30 September 2009. The red triangles are stations not in the well operational status in this time period. The black lines are faults. The gray line is the eye-center track of typhoon Morakot (Chen, 2009). The orange square is the HUALIAN-CWB weather station used in (j). The star and beach ball mark the location and focal mechanism solution of an M5.3 earthquake that occurred at 12.9-km depth on 28 June 2009, respectively. The red box marks the zone mentioned in Section 4.4. (b–h) The daily seismicity density maps on August 5–11, respectively. The bins are 20×20 km and colored by the number of events inside each bin on a day. (i) The average daily and cumulative rainfall in the target region (red box in a–h). (j) The atmospheric pressure recorded by the HUALIAN-CWB weather station (orange square in a) in these days (black bars, left vertical axis) and background seismicity rate (matched filter technique (MFT)-decluster) in the target region at depth of 0–15 km (red line, right vertical axis). (k) A zoom-in version of the latitude-time plot of seismicity in the red-box region in the Wu catalog. The full version is shown in Figure S3 in Supporting Information S1. The blue dashed line marks 7 August 2009. The red arrow marks the general migration of the seismicity. The open circles on the right outside mark earthquakes with different magnitudes. For example, "M1" means magnitude is equal to 1. (l) Similar to k but based on the MFT-reloc catalog.

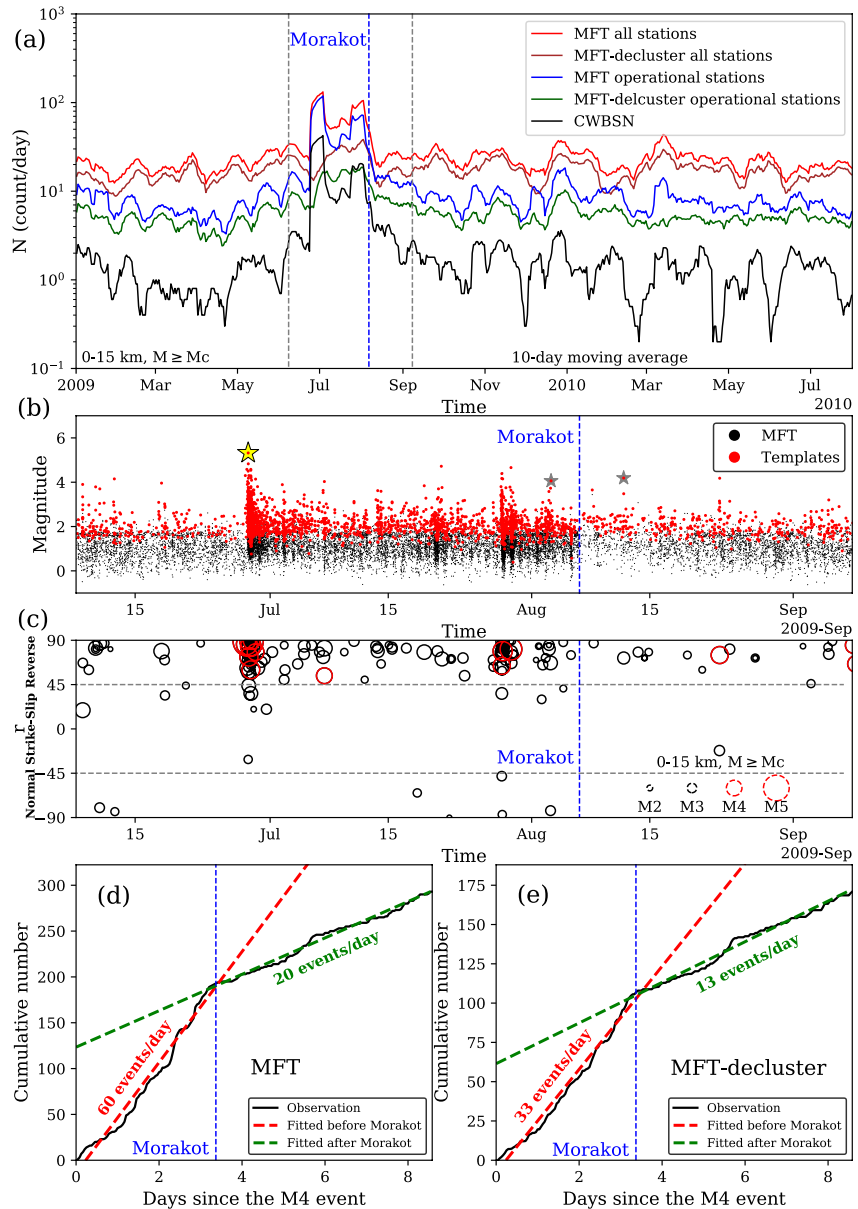


Figure 10. Seismicity in the zone near the eye-center track of typhoon Morakot (the red box in Figures 9a–9h). (a) The 10-day moving average seismicity rate at depth 0–15 km inside this zone. The blue dashed line marks 7 August 2009 (Figures 9k and 9l). The red and brown lines are the seismicity rate (above M_c) of the matched filter technique (MFT) catalog and the background seismicity rate of the MFT-decluster catalog using all stations, respectively. The blue and green lines are based on only using the operating stations (blue triangles in Figure 9a) instead of all stations to perform the earthquake detection. The black line is the result of CWBSN catalog. The two gray-dashed lines mark 1 June 2009 and 1 September 2009, respectively. (b) The magnitude-time distribution of seismicity at depth of 0–15 km inside the same space-time window. The yellow star marks the M5.3 earthquake, which is marked as the star and beachball in Figure 9a. The gray star on the left marks the last M4 earthquake in this zone before typhoon Morakot. The gray star on the right marks the first M4 earthquake in this zone after typhoon Morakot. (c) The time evolution of r -value of the seismicity listed in the MFT-FM catalog at depth of 0–15 km inside this zone between 1 June 2009 and 1 September 2009. $M < 4$ events are marked with black circles and $M \geq 4$ events are marked with red circles. (d) The cumulative number (black line) of events in the MFT catalog above the M_c at depth of 0–15 km inside this zone between the last M4 event before Morakot and the first M4 event after Morakot (two gray stars in b). The blue dashed line marks 7 August 2009. The red dashed line and green dashed line are the least squares regression results only using the data before Morakot and after Morakot, respectively. (e) Similar to (d), but based on the MFT-decluster catalog.

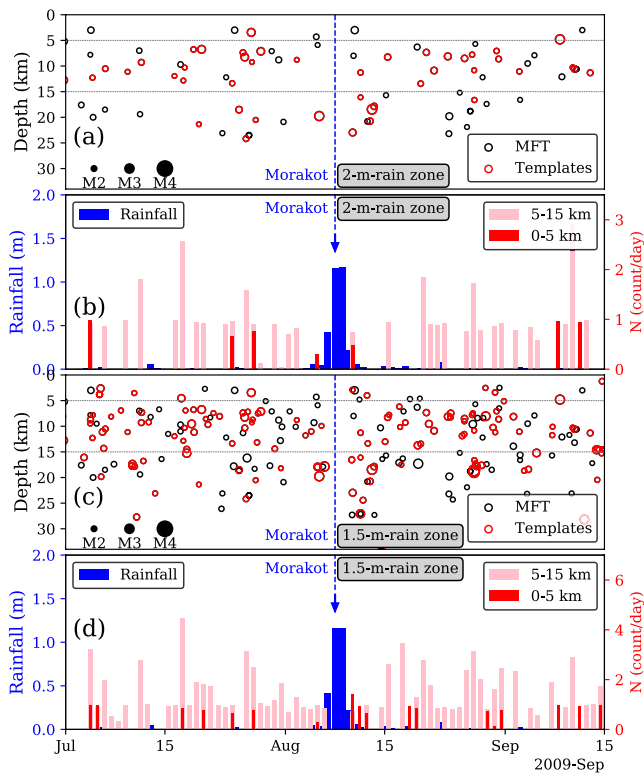


Figure 11. Seismicity in the heavy-rain zone from 5 weeks before to 5 weeks after typhoon Morakot. (a) The depth-time distribution of events (above M_c) in the matched filter technique (MFT) catalog and Wu catalog inside the heavy-rain zone, which is defined as the 2-m contour of the accumulated rainfall map (purple line in Figure 1). The blue dashed line marks the day typhoon Morakot landed in Taiwan (8 August 2009). The gray dashed lines mark the depth of 5 and 15 km used in (b). (b) The histogram of daily rainfall (blue vertical axis on the left, the bottom layer of the figure) and background seismicity rate (red vertical axis on the right, top layers of the figure) of MFT-decluster catalog at different depth ranges in the same zone and time period in (a). The daily rainfall data is recorded by the ALISHAN-CWB weather station in the heavy-rain zone (latitude: 23.5082°N; longitude: 120.8132°E; elevation: 2413.4 m). (c and d) are similar to (a and b), respectively. But the heavy-rain zone is redefined as the 1.5-m contour instead of the 2-m contour.

aftershock decay effect in our observed seismicity drop right after Morakot passage, we analyze the seismicity between the last M4 event before Morakot and the first M4 event after Morakot (two gray stars in Figure 10b) at depth of 0–15 km inside the target zone (the red box in Figures 9a–9h). Figures 10d and 10e show the time evolution of cumulative events number based on the events above M_c listed in the MFT and MFT-decluster catalog. We try to fit the data with modified Omori's law by using the AFTPOI package (Ogata, 2006), but it never converged. Nevertheless, the abrupt seismicity rate change before and after the typhoon is best explained as a reduction of rate by a factor of 3 (from 60 events/day to 20 events/day based on the MFT catalog or from 33 events/day to 13 events/day based on the MFT-decluster catalog). These two seismicity rates are calculated by using the least squares regression to fit the data before and after typhoon Morakot, respectively (Figures 10d and 10e).

4.5. Seismicity in the Heavy-Rain Zone in Weeks Before and After Morakot

To study possible influences of rainfall brought by typhoon Morakot on seismic activities, we analyze the seismicity in the heavy-rain zone in southern Taiwan (see the white line in Figure 1a). This zone is defined as the 2-m contour of the accumulated rainfall map of 5 days (6–10 August 2009) during typhoon Morakot (Figure 1). Because previous studies show that there is a ~10–13 days delay for rain-triggered earthquakes at depth of 0–5 km after the rainfall (Kraft et al., 2006; Svejdar et al., 2011), here we focus on the time scale of weeks around typhoon Morakot and separate the seismicity into 0–5 km and 5–15 km depth range. Comparing the seismicity rate in the five weeks before (Figure 11), there is a lack of earthquakes a few days during and after the heavy rain associated with typhoon Morakot. In addition, the seismicity fluctuated at depth ranges of 0–5 km and 5–15 km and we do not observe any clear changes in seismicity rates at these and larger depth ranges (Figures 11a and 11b). To rule out the influence of the way we define the heavy-rain zone, we also consider the 1.5-m contour instead of the 2-m contour. Based on the results with the 1.5-m heavy-rain zone (Figures 11c and 11d), we still do not observe any clear change of seismicity rate in southern Taiwan after the heavy rain brought by typhoon Morakot.

4.6. Seismicity in the Landslide Zone in Months Before and After Morakot

To study possible influences of landslides driven by typhoon Morakot and subsequent erosional processes on seismicity, we analyze the seismicity in the landslide zone (see the red line in Figure 1a) in a longer time scale of months before and after typhoon Morakot. This zone has a high spatial density of landslides triggered by typhoon Morakot, which is the same as defined in Steer et al. (2020). Here we examine three different aspects of seismicity patterns long before and after typhoon Morakot.

First, we compare the background seismicity rate at depth of 0–15 km in the landslide zone before and after typhoon Morakot (Figure 12). We focus on the shallow depth of 0–15 km, mostly because stress perturbations due to surface loading/unloading processes decrease significantly at larger depths (Steer et al., 2020; Tao et al., 2015). As shown in Figure 12, the background seismicity rates inside and outside of the landslide zones fluctuate, but both show a minor reduction at the time of typhoon Morakot. In addition, while the seismicity rate outside the landslide zone remains more or less stable, there is a gradual increase inside the landslide zone after typhoon Morakot.

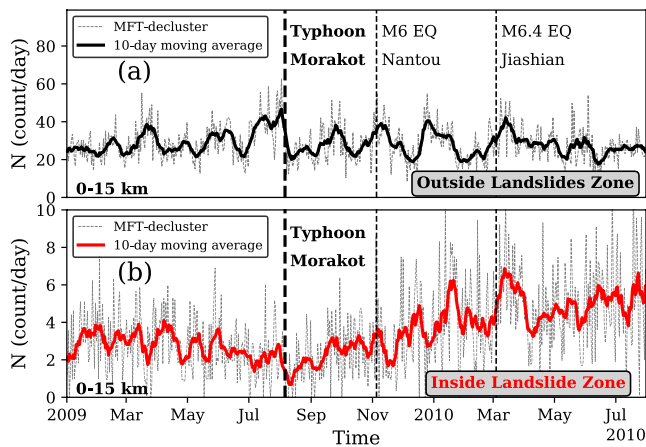


Figure 12. The background seismicity rate at depth of 0–15 km in the matched filter technique (MFT)-decluster catalog. (a and b) are the results of the events outside and inside the landslide zone (the red line in Figure 1a), respectively. The vertical black dashed lines mark the time of typhoon Morakot, the Nantou earthquake (outside but near the landslide zone at 24 km depth), and the Jiashian earthquake (inside the landslide zone at 22 km depth). These two M6+ earthquakes are marked as the yellow stars in Figure 1b. Note the depth range and the landslides zone are the same as those in Steer et al. (2020).

Second, we examine the Gutenberg-Richter b -value changes at different depths before and after typhoon Morakot with both the CWBSN and our MFT catalogs (not declustered). The results based on the CWBSN catalog show a subtle b -value increase at depth of 0–15 km in this landslide zone after typhoon Morakot (Figures 13b and 13f). This can match the results of Steer et al. (2020), which are also based on the CWBSN catalog in the same zone. However, the results based on our newly built MFT catalog do not show a clear b -value increase (Figures 13a and 13e). The results at depth 15–30 km are shown in Figure S5 in Supporting Information S1. The maps of b -value error, M_c , and the number of events used for computing the b -value map are shown in Figures S7–S14 of Supporting Information S1. To examine our b -value results at depth 0–15 km further, we calculate the b -value in two additional ways. We first consider the short-term incompleteness of the catalog after typhoon Morakot (Figure 8), and re-calculate the b -values by not using the first 3 weeks of seismicity. The updated results do not show a clear b -value increase (Figure S6 in Supporting Information S1). In addition, recently van der Elst (2021) proposed a more robust estimator of b -value termed b -positive (b^+) to reduce the effects of missing detections following a larger-magnitude event. Here we use this new method to re-calculate the b -values. The results with our newly built MFT catalog still do not show a clear b -value increase (Figures 13c and 13d).

Finally, we check temporal variations of earthquake focal mechanism solutions in the landslide zone using the MFT-FM catalog. We find a subtle decrease in the rate and percentage of normal-faulting events at depth of

0–15 km in this landslide zone after typhoon Morakot and before M6 Nantou Earthquake (Figures 14b–14d). To quantify the changing rates, we compute β -value and Z -value statistics mentioned before. We set the time window before Morakot starting from 1 January 2009 and the time window after Morakot ending on the day of the Nantou Earthquake (5 November 2009). Using the events at depth of 0–15 km in the landslide zone above M_c in the MFT-FM catalog, we obtain a β -value of -1.11 and a Z -value of -1.73 . Both values are below the significance threshold of 2.

5. Discussion

5.1. General Patterns of Seismicity Rate, Noise Energy, and Station Status

The number of events in our newly built MFT catalog is a seven-fold increase compared to the Wu catalog (templates) or the standard CWBSN catalog in our study period (19 months) (Figure 5). However, the number of detections for two weeks during and after typhoon Morakot (6–19 August 2009) is only a four-fold increase and there is a clear reduction of seismicity rate during and right after typhoon Morakot (Figures 8a and 8b). This is likely due to strong noises caused by wind and rainfall brought by typhoon Morakot. In addition, some stations were not working properly during and right after typhoon Morakot (Figures 8a and 8c). As expected, the noise level and the working status of stations have a greater impact on the detection capability of smaller earthquakes, because smaller earthquakes usually can be recorded by fewer nearby stations and have waveforms with low SNRs. This would result in miss-detection of small events, as marked by a triangle gap between magnitude -0.5 and 1 during and right after typhoon Morakot (Figure 8a). Similar gaps are found right after moderate to large earthquakes (Kagan, 2004; Peng et al., 2006). Although the MFT or other waveform-based techniques can help to detect some missing events in this gap (Peng & Zhao, 2009; Ross, Idini, et al., 2019; Yao et al., 2017), they cannot completely identify all small events that are either buried by the coda of larger aftershocks, or are not well recorded due to station outages.

5.2. Seismicity Near the Eye Center of Morakot in Days Before and After Morakot

As mentioned in Section 4.4, our results show a clear reduction of seismicity rate for a 40-day earthquake sequence at the time of typhoon passage in northeastern Taiwan (Figures 9 and 10). This observation is likely robust

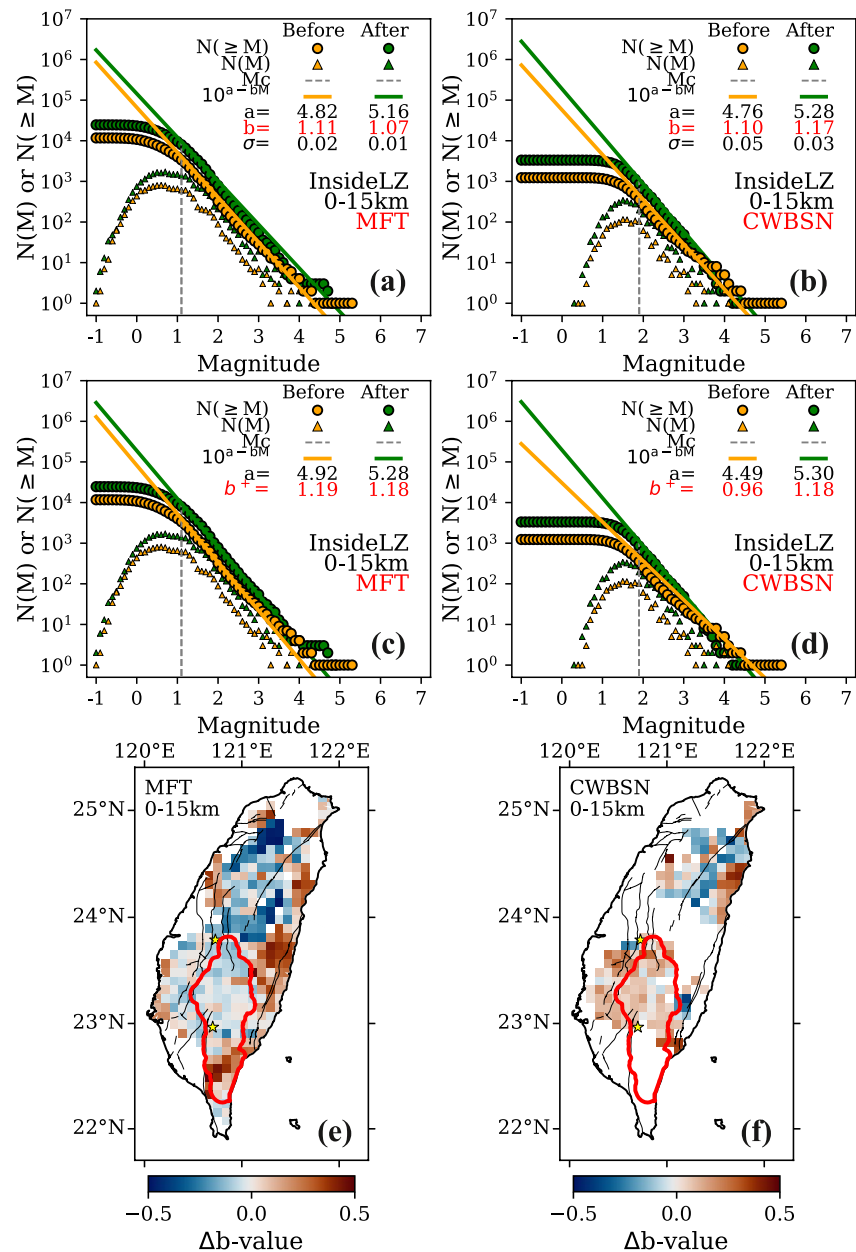


Figure 13. b -value variations by fitting the Gutenberg-Richter frequency-magnitude distribution. (a–b) The earthquake frequency-magnitude distribution and its corresponding b -value inside the landslide zone (marked by the red line in Figure 1a) of matched filter technique (MFT) catalog at 0–15 km depth, CWBSN catalog at 0–15 km depth, respectively. Orange data show the results before typhoon Morakot (1 January 2009–6 August 2009). Green data show the results after typhoon Morakot (7 August 2009–31 July 2010). (c–d) Similar to (a–b) but the b -value is calculated by using the b -positive method. (e–f) Change in b -value, Δb -value ($b_{\text{after}} - b_{\text{before}}$) based on the data in MFT catalog at 0–15 km depth, CWBSN catalog at 0–15 km depth, respectively. Grid steps are 10 km in both directions. The radius of the spatial window for each grid is set as 30 km. Black lines are the faults. The red line marks the boundary of the landslide zone (Figure 1). The two yellow stars are two magnitude (M) 6+ earthquakes (Figure 1) that occurred several months after typhoon Morakot (North: M6.0 Nantou earthquake on 5 November 2009, at 24 km depth; South: M6.4 Jiashian earthquake on 4 March 2010, at 22 km depth).

for the following two reasons. The first is that the results based on only using operating stations before and after typhoon Morakot are consistent with the results based on using all stations, as well as those based on the CWBSN catalog (Figure 10a). In addition, if the rate reduction was caused by increasing noise levels or station outages due to typhoon Morakot, we would expect that the seismicity rate returns back to the previous 40-day level right after

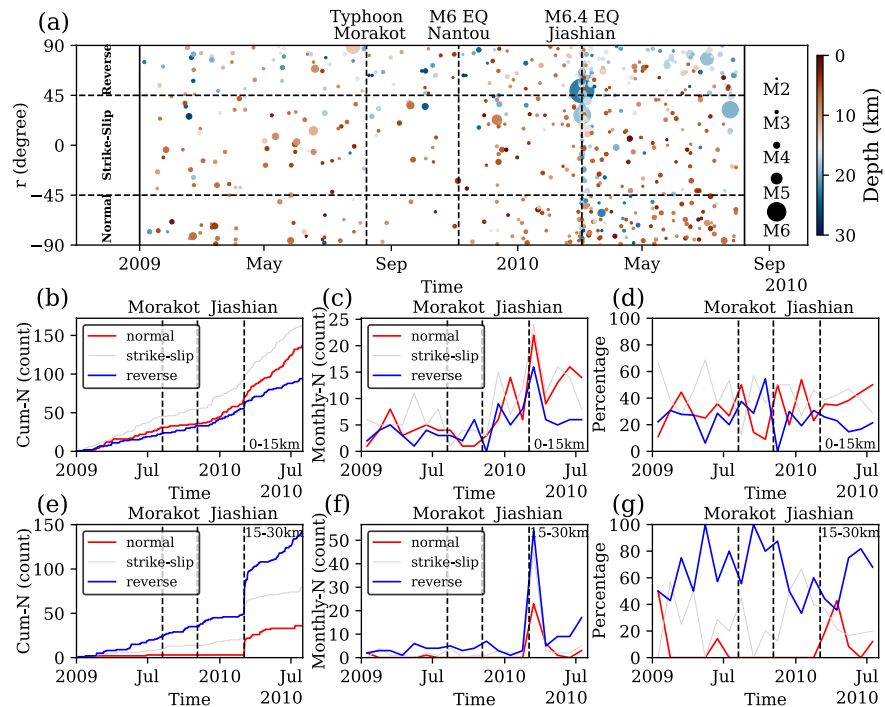


Figure 14. Temporal variations of earthquake focal mechanism solutions of the MFT-FM catalog inside the landslide zone. (a) The distribution of earthquakes' r -value over time. The r -value is the same as it in Figure 6, which is used to determine the faulting types of earthquakes. Horizontal dashed lines are boundaries between different faulting types. The vertical dashed lines mark the time of typhoon Morakot, the Nantou earthquake, and the Jiashian earthquake. Each dot is an earthquake colored by its depth and scaled by its magnitude. (b–d) The temporal variations of the cumulative number of earthquakes (b), seismicity rate of earthquakes (c), and percentages (d) for different types of earthquakes at depth of 0–15 km. (e, f, and g) are similar to (b, c, and d), respectively. But the depth range in (e, f, and g) are 15–30 km instead of 0–15 km.

the passage of typhoon Morakot. Instead, the seismicity rate reductions remained at the level before the 40-day sequence.

Our results also show that the observed seismicity rate reduction cannot be simply fitted and explained by Omori's law of aftershock decay (Figures 10d and 10e). Besides interpreting this phenomenon as a pure coincidence, one possible explanation is that the sudden reduction of seismicity rate is caused by the pass-by of typhoon Morakot. The lowest atmospheric pressure of the eye center of typhoon Morakot was 95.5 kPa when it was approaching this swarm zone on 7 August 2009 (Figure 9j and Figure S4 in Supporting Information S1). Compared to the standard atmosphere pressure (101.3 kPa), this pressure is 5.8 kPa lower, which is equivalent to the pressure caused by removing a 0.59-m thickness of water. A recent study in Taiwan shows that the average annual water thickness change in Taiwan is 0.53 m, which can result in Coulomb stress changes from 3 to 5 kPa on a 30°-dipping receiver thrust fault at 10-km depth in Taiwan (Hsu et al., 2020, 2021). Such level of Coulomb stress changes induced by hydrologic loading is capable of modulating seismicity in Taiwan and other regions (Bettinelli et al., 2008; Hsu et al., 2021; Johnson et al., 2017a, 2017b, 2020). Therefore, changing surface atmospheric pressure at Morakot's eye center can lead to a 3–5 kPa change of Coulomb stress on faults at ~10-km depth, capable of modulating the subsurface seismicity behavior. Besides the stress change caused by atmospheric pressure, the average cumulative rainfall during Morakot in this region is about 0.3 m (Figure 9i), which can lead to additional Coulomb stress change on the faults likely lower than 1–3 kPa.

When typhoon Morakot approached, a ground dilatation is expected due to atmospheric pressure drop and then followed by a larger ground compression due to rainfall loading and the recovery of ground deformation when the typhoon was away from northeastern Taiwan (Hsu et al., 2015; Mouyen et al., 2017). Therefore, reverse faulting events are prohibited by ground compression after typhoon Morakot (Figure 15). The focal mechanism solutions of earthquakes in this zone are diverse (Figure 6c), but most of them during the 40-day sequence are reverse-faulting events (Figures 9a and 10c). The nodal planes of the M5.2 earthquake (and other $M > 4$ events) show either

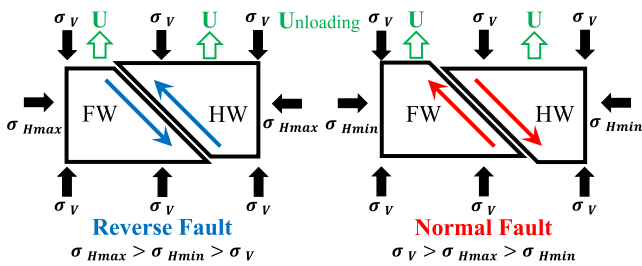


Figure 15. Directions and relative magnitudes of stresses for reverse fault and normal faults. FW and HW mark the footwall and hanging wall, respectively. Blue arrows and red arrows mark the direction of slip. Green arrows and U mark unloading. Black arrows mark the three principal axes of stresses: vertical (σ_v), maximum horizontal (σ_{Hmax}), and minimum horizontal (σ_{Hmin}).

NW dipping low-angle plane or high-angle dip-slip plane, consistent with the general subduction of the Philippine Sea Plate subducting under the Eurasian Plate and the Pacific Plate. Therefore, the seismicity rate reduction in this eye-center zone may be related to the increase of atmospheric pressure after the typhoon as well as the increase of water loading.

So far there are other two cases of seismic activities directly triggered by low-pressure systems of typhoons/hurricanes. The first is the aforementioned typhoon-triggered slow earthquakes in Eastern Taiwan (Liu et al., 2009), which was later interpreted as rainfall-induced strain changes (Hsu et al., 2015). The second is a transient increase of aftershocks following the 2011 M5.7 Virginia earthquake by Hurricane Irene (X. F. Meng et al., 2018). Here we observed a seismicity rate reduction coincide with typhoon Morakot, which is opposite of the rate increases observed in other two studies.

We note that our interpretation is rather speculative for the following reasons.

First, this could be a pure coincidence since an earthquake sequence can stop by itself. Second, the variation in atmospheric pressure and the loading effect from the rainfall and surface water is transient (within several days). Hence, we would expect that the seismicity returns back to the previous stage after days of typhoon Morakot, rather than remaining low following the typhoon. Future investigation of multiple typhoons by combining the local geodetic and seismology data, along with numerical modeling will be helpful to verify and reveal the detailed mechanism behind. Nevertheless, comparing with southern Taiwan at longer time scales, the seismicity reduction in northeastern Taiwan is the clearest seismicity rate change observed in this study.

5.3. Seismicity in the Heavy-Rain Zone in Weeks Before and After Morakot

Seismicity triggered by above-average rain and the following diffusion of ground water into subsurface structure has been observed in some regions, such as Switzerland, France, and Germany (Hainzl et al., 2006; Husen et al., 2007; Kraft et al., 2006; Rigo et al., 2008; Svejdar et al., 2011). As mentioned before, typhoon Morakot produced the highest rainfall in southern Taiwan in the recent 60 years (Chien & Kuo, 2011). It delivered up to 3 m of rainfall in the 5 days between August 6 and 10 August 2009 (Chen, 2009; Chien & Kuo, 2011). However, except for a lack of seismicity during typhoon Morakot's landfall, we did not observe any clear change of seismicity rate in the heavy-rain zone in southern Taiwan brought by typhoon Morakot (Figure 11).

Extreme rainfall could affect subsurface stress and seismicity in two ways. The first is an instantaneous loading effect on the surface. However, almost all seismic stations were not operating well in the several weeks during and after typhoon Morakot in the heavy-rain zone due to reasons such as power outages, equipment damages, or road damages (Figure 9a). Therefore, we do not have the resolution during the several days of heavy rainfall to examine the direct loading/unloading effect of rainfall on seismicity. The second possible effect of rainfall is the diffusion of rainwater into the subsurface structure, hence increasing pore pressure on active faults at seismogenic depth. We argue that this is less possible in the heavy-rain zone of this study, because Miller (2008) found that the rain-triggered earthquakes occurred exclusively in karst geology where the rainwater can quickly flow into the underground karst network to induce earthquakes. In this study, the heavy-rain zone is mainly in the southern Central Ranges with primarily metamorphic rocks where its permeability is much lower than the karst areas (Ho, 1988; Wang et al., 2004; Zhang, 2016). This is consistent with our observation that no clear changes in seismicity are observed in the following weeks in the heavy-rain zone either defined as the 2-m contour or the 1.5-m contour (Figures 1a and 11). We did not try to define the heavy-rain zone as the 1-m contour because the rainfall of many regions in both north and south Taiwan is above 1-m (Figure 1a), resulting in a much larger area as the target zone.

5.4. Seismicity in the Landslide Zone in Months Before and After Morakot

As mentioned in Section 4.6, our results based on the newly built MFT catalogs show a subtle increase in the background seismicity rate occurring in the next 12 months at depth of 0–15 km in the landslide zone after typhoon Morakot (Figure 12b), which match the observations of Steer et al. (2020) and Hsu et al. (2021) based

on the CWBSN catalog. Steer et al. (2020) attributed this to the crustal unloading caused by the intense and prolonged sediment erosion after typhoon Morakot in the landslide zone. Hsu et al. (2021) pointed out that another possible mechanism related to the interannual variation of terrestrial water storage, rather than the typhoon-associated landslides and erosions.

Steer et al. (2020) observed a clear b -value increase (Figure 13b) for seismicity at 0–15 km depth in the landslide zone over the 2.5 years after typhoon Morakot including the 1 year after typhoon Morakot in this study. However, we do not observe such a b -value increase in this study (Figure 13a). This is likely because that their results are based on the standard CWBSN catalog, which misses some small earthquakes. In this study, our results are based on the newly built MFT catalog, which is more complete than the standard CWBSN catalog. A recent study shows that some catalogs based on the matched filter technique in southern California and Italy do not preserve the exponential-like magnitude-frequency distribution toward low magnitudes (Herrmann & Marzocchi, 2021). This may lead to strong inconsistencies in b -values with different cutoff magnitudes. However, our study in Taiwan does not show a similar issue. For example, the b -values measured from the CWBSN catalog (with higher M_c) and our MFT catalog (with lower M_c) in the landslide zone before typhoon Morakot are very close: 1.11 and 1.10 (Figures 13a and 13b).

Another interesting phenomenon in the landslide zone is that the rate and percentage of normal-fault events and reverse-fault events at depths of 0–15 km moved toward two opposite trends following typhoon Morakot (Figures 14c and 14d). In particular, we found that the rate and percentage of normal-fault events decreased slightly after typhoon Morakot and before the M6 Nantou Earthquake (Figure 14b). This subtle change might be interpreted by the surface erosional unloading caused by the intense and rapid sediment transport in the several months right after typhoon Morakot in the landslide zone (Figure 15). The average erosion over the landslide zone in the following months after typhoon Morakot is about 2 cm (Chen et al., 2015; Steer et al., 2020). Steer et al. (2020) showed that 2–5 cm of average erosion can lead to about 2 kPa of Coulomb stress changes on a nearby fault at 5-km depth, which is roughly similar to the Coulomb stress changes induced by hydrologic loading/unloading that modulate seismicity in Taiwan and other regions (Bettinelli et al., 2008; Hsu et al., 2021; Johnson et al., 2017a, 2017b, 2020). The erosional unloading can reduce vertical stress (σ_v). For normal-fault events, this means the reduction of the difference between σ_v and σ_{Hmin} . Therefore, we expect to see fewer normal-fault events, which match our results shown in Figure 14. However, we note that the fluctuations of different types of events are relatively large in the entire study period (Figures 14c and 14d) and the seismicity rate change is below the significance threshold based on both β -value and Z -value statistics. Therefore, we conclude that even if such unloading affects microseismicity in this region, its effects are too small to be clearly observed (with statistical significance).

5.5. Lessons Learned and Their Implications for Future Studies

In this section, we briefly summarize lessons learned in this study, which we hope could be useful for similar future studies in other regions.

1. We use fixed thresholds (e.g., SNR and MAD) before, during, and after typhoon Morakot. However, during typhoon Morakot's passage, the background noise level was elevated, hence requiring signal with higher amplitudes in order to be detected (Figure 8). Such requirements reduce the ability to detect small earthquakes during these days, which prevents us from better understanding the short-term effects on local seismicity in central-southern Taiwan. In future studies, using a lower detection threshold during and right after typhoon may help, although this may introduce events that may not be genuine earthquakes. An alternative is to use methods such as deep-learning tools (e.g., Mousavi et al., 2020; Zhu et al., 2019) that may do not depend strongly on the SNR.
2. Although typhoon Morakot is the wettest typhoon in the past 60 years in Taiwan, it is relatively difficult to argue for a causal link between extreme weather events and earthquake activities based solely on observational results from a single event. To rule out the possibility of pure coincidence, it is best to examine many extreme weather events in the same region, or around the globe in order to better establish (or reject) their triggering relationship. If there are not enough such events available, detailed modeling studies can be helpful to interpret results from only a few cases (Jeandet Ribes et al., 2020; Steer et al., 2014).
3. Seismicity changes can be triggered by transient events such as another earthquake at nearby or teleseismic distances (Freed, 2005; Hill & Prejean, 2015), by both short-term (e.g., typhoons or hurricanes (X. F. Meng

Table 2
Summary of the Observations in This Study

Typhoon-Morakot-Driven surface process	Time scale	Space location	Observation of changes in seismicity
Atmospheric Pressure Variation at Eye Center	Hours-Days	Northeastern Taiwan	Yes, and statistically significant
Heavy Rainfall	Days-Weeks	Central-Southern Taiwan	Unmeasurable
Landslide Erosion	Months-Years	Central-Southern Taiwan	Yes, but not significant

et al., 2018)) and long-term (e.g., annual and internal hydrological loading/unloading (Hsu et al., 2021) processes, in addition to regular tectonic loading. Hence, it is important to separate the effects from long-term changes on seismicity rate changes first, before analyzing any short-term effects due to extreme weather events.

- There is an intrinsic difficulty in observing seismicity change in the presence of high seismic noises and station outages like the time period during and right after typhoon Morakot. For future similar studies, focusing on regions with borehole seismic stations (e.g., the HiNet in Japan) could help to at least suppress the recording of surface seismic noises associated with extreme weather events.

6. Conclusions

By using the matched filter technique, we build a more complete earthquake catalog for Taiwan spanning 7 months before and 12 months after the 2009 typhoon Morakot, which brought the highest rainfall in southern Taiwan in the past 60 years. The number of events in our newly built catalog is a seven-fold increase compared to the standard CWBSN catalog. We also relocate the detected events and calculate their focal mechanism solutions based on first-motion polarities from a deep-learning model. With our newly built catalogs, we analyze possible effects of typhoon Morakot on the seismicity in Taiwan from three aspects (Table 2). First, we find that the seismicity rate of a 40-day earthquake sequence in northeastern Taiwan was reduced significantly right following the passage of typhoon Morakot's eye center. This phenomenon may be related to the increase of atmospheric pressure after the typhoon as well as the increase of water loading. Second, we do not observe any clear change of seismicity rate in the heavy-rain zone in the following five weeks after the rainfall brought by typhoon Morakot. This is likely due to strong noise and station outages during and right after typhoon Morakot. Finally, at depths of 0–15 km in the typhoon-triggered landslide zone in southern Taiwan, we find a slight increase in background seismicity rate occurring in the next 12 months after typhoon Morakot, which can match the results of a recent study (Steer et al., 2020) arguing for surface unloading due to sediment transport following typhoon Morakot. However, such a feature could also be explained by the interannual variation of terrestrial water storage (Hsu et al., 2021). We do not observe a clear change in the Gutenberg-Richter b -value in the landslide zone in southern Taiwan for seismicity at 0–15 km, which is different from the Steer et al. (2020) results based on a previous and less complete CWBSN catalog. However, there is a clear b -value reduction in southern Taiwan for seismicity at 15–30 km, which would be difficult to interpret as surface loading/unloading effects. Overall, except for a reduction in seismicity rate near the typhoon's low-pressure eye center in northeastern Taiwan, we do not observe other clear seismicity changes that can be attributed to surface changes induced by typhoon Morakot. A systematic examination of multiple typhoons in Taiwan or extreme weather events around the globe may help us to ultimately answer the question of whether extreme weather events at the surface can trigger or suppress earthquakes at seismogenic depth.

Conflict of Interest

The authors declare no conflicts of interest relevant to this study.

Data Availability Statement

Detailed information on how to access seismic and metrological data can be found in the Supporting Information S1. The earthquake catalogs (MFT, MFT-reloc, and MFT-FM catalogs) used in this study are available through the Mendeley Data (<https://dx.doi.org/10.17632/cgys3svzrp.1> (Zhai et al., 2021)). The original Wu

earthquake catalogs (Wu, Chang, et al., 2008a; Wu, Zhao, et al., 2008) and the 3D velocity model of Taiwan (Wu et al., 2007) used in this study are archived in the Seismological Lab at National Taiwan University (<http://seismology.gi.ntu.edu.tw/download.htm>, last accessed November 2021). Some figures are plotted by using the Generic Mapping Tools (Wessel et al., 2013), Version 5.4.1 (<https://www.generic-mapping-tools.org/>, last accessed November 2021).

Acknowledgments

The authors thank Central Weather Bureau for providing the raw waveforms, CWBSN earthquake catalog and phase picks. The authors thank Kevin Chao for his help in preparing the raw seismic data. The authors also thank two anonymous reviewers, the associate editor, and editor Rachel Abercrombie for their constructive comments, which help us improve the manuscript. This study used the Comet GPU cluster in the Extreme Science and Engineering Discovery Environment (XSEDE), which is supported by National Science Foundation (NSF, grant number OCI-1053575). This study was supported by National Aeronautics and Space Administration (NASA, grant number 80NS-SC17K0098). This is contribution number 1380 from the Institute of Environment at Florida International University.

References

- Aki, K. (1965). Maximum likelihood estimate of b in the Formula $\log N = a - bM$ and its confidence limits. *Bulletin of the Earthquake Research Institute University of Tokyo*, 43(2), 237–239.
- Bettinelli, P., Avouac, J. P., Flouzat, M., Bollinger, L., Ramillien, G., Rajaure, S., & Sapkota, S. (2008). Seasonal variations of seismicity and geodetic strain in the Himalaya induced by surface hydrology. *Earth and Planetary Science Letters*, 266(3–4), 332–344. <https://doi.org/10.1016/j.epsl.2007.11.021>
- Bonilla, M. G., Mark, R. K., & Lienkaemper, J. J. (1984). Statistical Relations among earthquake magnitude, surface rupture length, and surface fault displacement. *Bulletin of the Seismological Society of America*, 74(6), 2379–2411. <https://doi.org/10.3133/ofr84256>
- Calais, E., Freed, A. M., Van Arsdale, R., & Stein, S. (2010). Triggering of new Madrid seismicity by late-Pleistocene erosion. *Nature*, 466(7306), 608–611. <https://doi.org/10.1038/nature09258>
- Chamberlain, C. J., Hopp, C. J., Boese, C. M., Warren-Smith, E., Chambers, D., Chu, S. X., et al. (2017). EQcorrscan: Repeating and near-repeating earthquake detection and analysis in python. *Seismological Research Letters*, 89(1), 173–181. <https://doi.org/10.1785/0220170151>
- Chang, C. H., Wu, Y. M., Zhao, L., & Wu, F. T. (2007). Aftershocks of the 1999 Chi-Chi, Taiwan, earthquake: The first hour. *Bulletin of the Seismological Society of America*, 97(4), 1245–1258. <https://doi.org/10.1785/0120060184>
- Chen, Y. (2009). *Report on typhoon morakot (0908) of 2009*. Weather Forecast Center Central Weather Bureau. Ministry of Interior.
- Chen, Y. C., Chang, K. T., Lee, H. Y., & Chiang, S. H. (2015). Average landslide erosion rate at the watershed scale in southern Taiwan estimated from magnitude and frequency of rainfall. *Geomorphology*, 228, 756–764. <https://doi.org/10.1016/j.geomorph.2014.07.022>
- Cheng, Y. F., & Ben-Zion, Y. (2020). Variations of earthquake properties before, during, and after the 2019 M7.1 Ridgecrest, CA, Earthquake. *Geophysical Research Letters*, 47. <https://doi.org/10.1029/2020GL089650>
- Chien, F. C., & Kuo, H. C. (2011). On the extreme rainfall of Typhoon Morakot (2009). *Journal of Geophysical Research*, 116. <https://doi.org/10.1029/2010jd015092>
- Costain, J. K., & Bollinger, G. A. (2010). Review: Research results in hydroseismicity from 1987 to 2009. *Bulletin of the Seismological Society of America*, 100, 1841–1858. <https://doi.org/10.1785/0120090288>
- Dadson, S. J., Hovius, N., Chen, H., Dade, W. B., Hsieh, M. L., Willett, S. D., et al. (2003). Links between erosion, runoff variability and seismicity in the Taiwan orogen. *Nature*, 426(6967), 648–651. <https://doi.org/10.1038/nature02150>
- Enescu, B., Mori, J., & Miyazawa, M. (2007). Quantifying early aftershock activity of the 2004 mid-Niigata Prefecture earthquake (Mw6.6). *Journal of Geophysical Research*, 112. <https://doi.org/10.1029/2006jb004629>
- Freed, A. M. (2005). Earthquake triggering by static, dynamic, and postseismic stress transfer. *Annual Review of Earth and Planetary Sciences*, 33(1), 335–367. <https://doi.org/10.1146/annurev.earth.33.092203.122505>
- Gao, S. S., Silver, P. G., Linde, A. T., & Sacks, I. S. (2000). Annual modulation of triggered seismicity following the 1992 Landers earthquake in California. *Nature*, 406(6795), 500–504. <https://doi.org/10.1038/35020045>
- Gardner, J., & Knopoff, L. (1974). Is the sequence of earthquakes in Southern California, with aftershocks removed, Poissonian? *Bulletin of the Seismological Society of America*, 64(5), 1363–1367. <https://doi.org/10.1785/bssa0640051363>
- Gibbons, S. J., & Ringdal, F. (2006). The detection of low magnitude seismic events using array-based waveform correlation. *Geophysical Journal International*, 165(1), 149–166. <https://doi.org/10.1111/j.1365-246X.2006.02865.x>
- Grollimund, B., & Zoback, M. D. (2001). Did deglaciation trigger intraplate seismicity in the New Madrid seismic zone? *Geology*, 29(2), 175–178. [https://doi.org/10.1130/0091-7613\(2001\)029<0175:DDTISI>2.0.CO;2](https://doi.org/10.1130/0091-7613(2001)029<0175:DDTISI>2.0.CO;2)
- Gutenberg, B. (1956). The energy of earthquakes. *Quarterly Journal of the Geological Society*, 112(1–4), 1–6. https://doi.org/10.1007/978-3-662-28668-5_1
- Gutenberg, B., & Richter, C. F. (1944). Frequency of earthquakes in California. *Bulletin of the Seismological Society of America*, 34(4), 185–188. <https://doi.org/10.1785/bssa0340040185>
- Habermann, R. (1981). Precursory seismicity patterns: Stalking the mature seismic gap. *Earthquake Prediction: An International Review*, 4, 29–42.
- Habermann, R. E. (1983). Teleseismic detection in the Aleutian island-arc. *Journal of Geophysical Research*, 88, 5056–5064. <https://doi.org/10.1029/JB088iB06p05056>
- Hainzl, S., Ben-Zion, Y., Cattania, C., & Wassermann, J. (2013). Testing atmospheric and tidal earthquake triggering at Mt. Hochstaufen, Germany. *Journal of Geophysical Research: Solid Earth*, 118, 5442–5452. <https://doi.org/10.1002/jgrb.50387>
- Hainzl, S., Kraft, T., Wassermann, J., Igel, H., & Schmedes, E. (2006). Evidence for rainfall-triggered earthquake activity. *Geophysical Research Letters*, 33. <https://doi.org/10.1029/2006gl027642>
- Hara, S., Fukahata, Y., & Iio, Y. (2019). P-wave first-motion polarity determination of waveform data in western Japan using deep learning. *Earth Planets and Space*, 71(1). <https://doi.org/10.1186/s40623-019-1111-x>
- Heki, K. (2001). Seasonal modulation of interseismic strain buildup in northeastern Japan driven by snow loads. *Science*, 293(5527), 89–92. <https://doi.org/10.1126/science.1061056>
- Heki, K. (2003). Snow load and seasonal variation of earthquake occurrence in Japan. *Earth and Planetary Science Letters*, 207(1–4), 159–164. [https://doi.org/10.1016/S0012-821x\(02\)01148-2](https://doi.org/10.1016/S0012-821x(02)01148-2)
- Herrmann, M., & Marzocchi, W. (2021). Inconsistencies and lurking pitfalls in the magnitude-frequency distribution of high-resolution earthquake catalogs. *Seismological Research Letters*, 92(2), 909–922. <https://doi.org/10.1785/0220200337>
- Hill, D. P., & Prejean, S. G. (2015). Dynamic triggering. In *Treatise on Geophysics* (pp. 273–304). Elsevier. <https://doi.org/10.1016/b978-0-444-53802-4.00078-6>
- Ho, C.-S. (1988). *An introduction to the geology of Taiwan, explanatory text of the geologic map of Taiwan* (pp. 151–152). Central Geological Survey.

- Hsu, Y. J., Chang, Y. S., Liu, C. C., Lee, H. M., Linde, A. T., Sacks, S. I., et al. (2015). Revisiting borehole strain, typhoons, and slow earthquakes using quantitative estimates of precipitation-induced strain changes. *Journal of Geophysical Research: Solid Earth*, 120, 4556–4571. <https://doi.org/10.1002/2014jb011807>
- Hsu, Y. J., Fu, Y. N., Burgmann, R., Hsu, S. Y., Lin, C. C., Tang, C. H., & Wu, Y. M. (2020). Assessing seasonal and interannual water storage variations in Taiwan using geodetic and hydrological data. *Earth and Planetary Science Letters*, 550, 116532. <https://doi.org/10.1016/j.epsl.2020.116532>
- Hsu, Y. J., Kao, H., Burgmann, R., Lee, Y. T., Huang, H. H., Hsu, Y. F., et al. (2021). Synchronized and asynchronous modulation of seismicity by hydrological loading: A case study in Taiwan. *Science Advance*, 7(16), eabf7282. <https://doi.org/10.1126/sciadv.abf7282>
- Hung, C., Lin, G. W., Kuo, H. L., Zhang, J. M., Chen, C. W., & Chen, H. (2018). Impact of an extreme typhoon event on subsequent sediment discharges and rainfall-driven landslides in affected mountainous regions of Taiwan. *Geofluids*, 2018, 1–11. <https://doi.org/10.1155/2018/8126518>
- Husen, S., Bachmann, C., & Giardini, D. (2007). Locally triggered seismicity in the central Swiss Alps following the large rainfall event of August 2005. *Geophysical Journal International*, 171(3), 1126–1134. <https://doi.org/10.1111/j.1365-246X.2007.03561.x>
- Jeandet Ribes, L., Cubas, N., Bhat, H. S., & Steer, P. (2020). The impact of large erosional events and transient normal stress changes on the seismicity of faults. *Geophysical Research Letters*, 47. <https://doi.org/10.1029/2020gl087631>
- Johnson, C. W., Fu, Y., & Burgmann, R. (2017). Seasonal water storage, stress modulation, and California seismicity. *Science*, 356(6343), 1161–1164. <https://doi.org/10.1126/science.aak9547>
- Johnson, C. W., Fu, Y. N., & Burgmann, R. (2017). Stress models of the annual hydrospheric, atmospheric, thermal, and tidal loading cycles on California Faults: Perturbation of background stress and changes in seismicity. *Journal of Geophysical Research: Solid Earth*, 122, 10605–10625. <https://doi.org/10.1002/2017jb014778>
- Johnson, C. W., Fu, Y. N., & Burgmann, R. (2020). Hydrospheric modulation of stress and seismicity on shallow faults in southern Alaska. *Earth and Planetary Science Letters*, 530, 115904. <https://doi.org/10.1016/j.epsl.2019.115904>
- Kagan, Y. Y. (2004). Short-term properties of earthquake catalogs and models of earthquake source. *Bulletin of the Seismological Society of America*, 94(4), 1207–1228. <https://doi.org/10.1785/012003098>
- Keefer, D. K. (2002). Investigating landslides caused by earthquakes - A historical review. *Surveys in Geophysics*, 23(6), 473–510. <https://doi.org/10.1023/A:1021274710840>
- Khazai, B., & Sitar, N. (2004). Evaluation of factors controlling earthquake-induced landslides caused by Chi-Chi earthquake and comparison with the Northridge and Loma Prieta events. *Engineering Geology*, 71(1–2), 79–95. [https://doi.org/10.1016/S0013-7952\(03\)00127-3](https://doi.org/10.1016/S0013-7952(03)00127-3)
- Kraft, T., Wassermann, J., & Igel, H. (2006). High-precision relocation and focal mechanism of the 2002 rain-triggered earthquake swarms at Mt Hochstaufen, SE Germany. *Geophysical Journal International*, 167(3), 1513–1528. <https://doi.org/10.1111/j.1365-246X.2006.03171.x>
- Lei, X. L. (2011). Possible roles of the Zipingpu Reservoir in triggering the 2008 Wenchuan earthquake. *Journal of Asian Earth Sciences*, 40(4), 844–854. <https://doi.org/10.1016/j.jseas.2010.05.004>
- Lin, C. H. (2005). Seismicity increase after the construction of the world's tallest building: An active blind fault beneath the Taipei 101. *Geophysical Research Letters*, 32. <https://doi.org/10.1029/2005gl024223>
- Lin, C. H., Jan, J. C., Pu, H. C., Tu, Y., Chen, C. C., & Wu, Y. M. (2015). Landslide seismic magnitude. *Earth and Planetary Science Letters*, 429, 122–127. <https://doi.org/10.1016/j.epsl.2015.07.068>
- Lin, C.-W., Chang, W.-S., Liu, S.-H., Tsai, T.-T., Lee, S.-P., Tsang, Y.-C., et al. (2011). Landslides triggered by the 7 August 2009 Typhoon Morakot in southern Taiwan. *Engineering Geology*, 123(1–2), 3–12. <https://doi.org/10.1016/j.enggeo.2011.06.007>
- Lin, G. Q. (2020). Waveform cross-correlation relocation and focal mechanisms for the 2019 Ridgecrest earthquake sequence. *Seismological Research Letters*, 91(4), 2055–2061. <https://doi.org/10.1785/0220190277>
- Lin, J. W. (2013). An empirical correlation between the occurrence of earthquakes and typhoons in Taiwan: A statistical multivariate approach. *Natural Hazards*, 65(1), 605–634. <https://doi.org/10.1007/s11069-012-0382-3>
- Liu, C., Linde, A. T., & Sacks, I. S. (2009). Slow earthquakes triggered by typhoons. *Nature*, 459(7248), 833–836. <https://doi.org/10.1038/nature08042>
- Manga, M., & Brodsky, E. (2006). Seismic triggering of eruptions in the far field: Volcanoes and geysers. *Annual Review of Earth and Planetary Sciences*, 34(1), 263–291. <https://doi.org/10.1146/annurev.earth.34.031405.125125>
- Maniatis, G., Kurfess, D., Hampel, A., & Heidbach, O. (2009). Slip acceleration on normal faults due to erosion and sedimentation - Results from a new three-dimensional numerical model coupling tectonics and landscape evolution. *Earth and Planetary Science Letters*, 284(3–4), 570–582. <https://doi.org/10.1016/j.epsl.2009.05.024>
- Matthews, M. V., & Reasenberg, P. A. (1988). Statistical methods for investigating quiescence and other temporal seismicity patterns. *Pure and Applied Geophysics*, 126(2–4), 357–372. <https://doi.org/10.1007/Bf00879003>
- McGarr, A., Simpson, D., Seeber, L., & Lee, W. (2002). Case histories of induced and triggered seismicity. *International Geophysics Series*, 81(A), 647–661. [https://doi.org/10.1016/s0074-6142\(02\)80243-1](https://doi.org/10.1016/s0074-6142(02)80243-1)
- Meng, X., & Peng, Z. (2014). Seismicity rate changes in the Salton Sea Geothermal Field and the San Jacinto Fault Zone after the 2010 Mw 7.2 El Mayor-Cucapah earthquake. *Geophysical Journal International*, 197(3), 1750–1762. <https://doi.org/10.1093/gji/ggu085>
- Meng, X., Yu, X., Peng, Z., & Hong, B. (2012). Detecting Earthquakes around Salton Sea Following the 2010 Mw7.2 El Mayor-Cucapah Earthquake Using GPU Parallel Computing. *Procedia Computer Science*, 9, 937–946. <https://doi.org/10.1016/j.procs.2012.04.100>
- Meng, X. F., Yang, H. F., & Peng, Z. G. (2018). Foreshocks, b Value Map, and Aftershock Triggering for the 2011 M-w 5.7 Virginia Earthquake. *Journal of Geophysical Research: Solid Earth*, 123, 5082–5098. <https://doi.org/10.1029/2017jb015136>
- Miller, S. A. (2008). Note on rain-triggered earthquakes and their dependence on karst geology. *Geophysical Journal International*, 173(1), 334–338. <https://doi.org/10.1111/j.1365-246X.2008.03735.x>
- Mousavi, S. M., Ellsworth, W. L., Zhu, W., Chuang, L. Y., & Beroza, G. C. (2020). Earthquake transformer-an attentive deep-learning model for simultaneous earthquake detection and phase picking. *Nature Communications*, 11(1), 3952. <https://doi.org/10.1038/s41467-020-17591-w>
- Mouyen, M., Canitano, A., Chao, B. F., Hsu, Y. J., Steer, P., Longuevergne, L., & Boy, J. P. (2017). Typhoon-induced ground deformation. *Geophysical Research Letters*, 44, 11004–11011. <https://doi.org/10.1002/2017gl075615>
- Ogata, Y. (1988). Statistical models for earthquake occurrences and residual analysis for point-processes. *Journal of the American Statistical Association*, 83(401), 9–27. <https://doi.org/10.1080/01621459.1988.10478560>
- Ogata, Y. (2006). *Statistical analysis of seismicity: Updated version (SASeis2006)*. Institute of Statistical Mathematics.
- Pankow, K. L., & Kilb, D. (2020). Going beyond rate changes as the sole indicator for dynamic triggering of earthquakes. *Scientific Reports*, 10(1), 4120. <https://doi.org/10.1038/s41598-020-60988-2>
- Peltzer, G., Rosen, P., Rogez, F., & Hudnut, K. (1998). Porolastic rebound along the Landers 1992 earthquake surface rupture. *Journal of Geophysical Research*, 103(B12), 30131–30145. <https://doi.org/10.1029/98jb02302>

- Peng, Z. G., Vidale, J. E., & Houston, H. (2006). Anomalous early aftershock decay rate of the 2004 Mw6.0 Parkfield, California, earthquake. *Geophysical Research Letters*, 33. <https://doi.org/10.1029/2006gl026744>
- Peng, Z. G., & Zhao, P. (2009). Migration of early aftershocks following the 2004 Parkfield earthquake. *Nature Geoscience*, 2(12), 877–881. <https://doi.org/10.1038/ngeo697>
- Prejean, S. G., & Hill, D. P. (2018). The influence of tectonic environment on dynamic earthquake triggering: A review and case study on Alaskan volcanoes. *Tectonophysics*, 745, 293–304. <https://doi.org/10.1016/j.tecto.2018.08.007>
- Qian, Y. Y., Chen, X. F., Luo, H., Wei, S. J., Wang, T., Zhang, Z. G., & Luo, X. Y. (2019). An extremely shallow M(w)4.1 thrust earthquake in the Eastern Sichuan Basin (China) likely triggered by unloading during infrastructure construction. *Geophysical Research Letters*, 46, 13775–13784. <https://doi.org/10.1029/2019gl085199>
- Reasenber, P. A., & Simpson, R. W. (1992). Response of regional seismicity to the static stress change produced by the loma prieta earthquake. *Science*, 255(5052), 1687–1690. <https://doi.org/10.1126/science.255.5052.1687>
- Rigo, A., Bethoux, N., Masson, F., & Ritz, J. F. (2008). Seismicity rate and wave-velocity variations as consequences of rainfall: The case of the catastrophic storm of September 2002 in the Nîmes Fault region (Gard, France). *Geophysical Journal International*, 173(2), 473–482. <https://doi.org/10.1111/j.1365-246X.2008.03718.x>
- Rodriguez, C., Bommer, J., & Chandler, R. (1999). Earthquake-induced landslides: 1980–1997. *Soil Dynamics and Earthquake Engineering*, 18(5), 325–346.
- Ross, Z. E., Idini, B., Jia, Z., Stephenson, O. L., Zhong, M., Wang, X., et al. (2019). Hierarchical interlocked orthogonal faulting in the 2019 Ridgecrest earthquake sequence. *Science*, 366(6463), 346–351. <https://doi.org/10.1126/science.aaz0109>
- Ross, Z. E., Meier, M.-A., & Hauksson, E. (2018). PWave arrival picking and first-motion polarity determination with deep learning. *Journal of Geophysical Research: Solid Earth*, 123, 5120–5129. <https://doi.org/10.1029/2017jb015251>
- Ross, Z. E., Trugman, D. T., Hauksson, E., & Shearer, P. M. (2019). Searching for hidden earthquakes in Southern California. *Science*, 364(6442), 767–771. <https://doi.org/10.1126/science.aaw6888>
- Roth, P., Pavoni, N., & Deichmann, N. (1992). Seismotectonics of the Eastern Swiss Alps and evidence for precipitation-induced variations of seismic activity. *Tectonophysics*, 207(1–2), 183–197. [https://doi.org/10.1016/0040-1951\(92\)90477-N](https://doi.org/10.1016/0040-1951(92)90477-N)
- Shearer, P. M., Prieto, G. A., & Hauksson, E. (2006). Comprehensive analysis of earthquake source spectra in southern California. *Journal of Geophysical Research*, 111(B6). <https://doi.org/10.1029/2005jb003979>
- Shelly, D. R., Beroza, G. C., & Ide, S. (2007). Non-volcanic tremor and low-frequency earthquake swarms. *Nature*, 446(7133), 305–307. <https://doi.org/10.1038/nature05666>
- Shelly, D. R., Ellsworth, W. L., & Hill, D. P. (2016). Fluid-faulting evolution in high definition: Connecting fault structure and frequency-magnitude variations during the 2014 Long Valley Caldera, California, earthquake swarm. *Journal of Geophysical Research: Solid Earth*, 121, 1776–1795. <https://doi.org/10.1002/2015jb012719>
- Shelly, D. R., Hardebeck, J. L., Ellsworth, W. L., & Hill, D. P. (2016). A new strategy for earthquake focal mechanisms using waveform-correlation-derived relative polarities and cluster analysis: Application to the 2014 Long Valley Caldera earthquake swarm. *Journal of Geophysical Research: Solid Earth*, 121, 8622–8641. <https://doi.org/10.1002/2016jb013437>
- Shin, T. (1992). Some implications of Taiwan tectonic features from the data collected by the Central Weather Bureau Seismic Network. *Meteorol. Bull.*, 38, 23–48. (in Chinese).
- Shyu, J. B. H., Chuang, Y. R., Chen, Y. L., Lee, Y. R., & Cheng, C. T. (2016). A new on-land seismogenic structure source database from the Taiwan Earthquake Model (TEM) project for seismic hazard analysis of Taiwan. *Terrestrial Atmospheric and Oceanic Sciences*, 27(3), 311–323. [https://doi.org/10.3319/tao.2015.11.27.02\(tem\)](https://doi.org/10.3319/tao.2015.11.27.02(tem))
- Steer, P., Jeandet, L., Cubas, N., Marc, O., Meunier, P., Simoes, M., et al. (2020). Earthquake statistics changed by typhoon-driven erosion. *Scientific Reports*, 10(1), 10899. <https://doi.org/10.1038/s41598-020-67865-y>
- Steer, P., Simoes, M., Cattin, R., & Shyu, J. B. (2014). Erosion influences the seismicity of active thrust faults. *Nature Communications*, 5(1), 5564. <https://doi.org/10.1038/ncomms6564>
- Svejdar, V., Kuchenhoff, H., Fahrmeir, L., & Wassermann, J. (2011). External forcing of earthquake swarms at Alpine regions: Example from a seismic meteorological network at Mt. Hochstaufen SE-Bavaria. *Nonlinear Processes in Geophysics*, 18(6), 849–860. <https://doi.org/10.5194/npg-18-849-2011>
- Tao, W., Masterlark, T., Shen, Z. K., & Ronchin, E. (2015). Impoundment of the Zipingpu reservoir and triggering of the 2008 Mw 7.9 Wenchuan earthquake, China. *Journal of Geophysical Research: Solid Earth*, 120, 7033–7047. <https://doi.org/10.1002/2014JB011766>
- Thorson, R. M. (1996). Earthquake recurrence and glacial loading in western Washington. *Geological Society of America Bulletin*, 108(9), 1182–1191. [https://doi.org/10.1130/0016-7606\(1996\)108<1182:eragli>2.3.co;2](https://doi.org/10.1130/0016-7606(1996)108<1182:eragli>2.3.co;2)
- Trugman, D. T., & Shearer, P. M. (2017). GrowClust: A hierarchical clustering algorithm for relative earthquake relocation, with application to the Spanish springs and sheldon, Nevada, earthquake sequences. *Seismological Research Letters*, 88(2), 379–391. <https://doi.org/10.1785/0220160188>
- Tsai, Y.-B. (1986). Seismotectonics of Taiwan. *Tectonophysics*, 125(1–3), 17–37. [https://doi.org/10.1016/0040-1951\(86\)90005-3](https://doi.org/10.1016/0040-1951(86)90005-3)
- Uchide, T. (2020). Focal mechanisms of small earthquakes beneath the Japanese islands based on first-motion polarities picked using deep learning. *Geophysical Journal International*, 223(3), 1658–1671. <https://doi.org/10.1093/gji/egaa401>
- Utsu, T., Ogata, Y., Matsuura, R. S., & Matsu'ura (1995). The centenary of the omori formula for a decay law of aftershock Activity. *Journal of Physics of the Earth*, 43(1), 1–33. <https://doi.org/10.4294/jpe1952.43.1>
- van der Elst, N. J. (2021). B-Positive: A robust estimator of aftershock magnitude distribution in transiently incomplete catalogs. *Journal of Geophysical Research: Solid Earth*, 126. <https://doi.org/10.1029/2020jb021027>
- Waldhauser, F., & Ellsworth, W. L. (2000). A double-difference earthquake location algorithm: Method and application to the northern Hayward fault, California. *Bulletin of the Seismological Society of America*, 90(6), 1353–1368. <https://doi.org/10.1785/0120000006>
- Wang, C.-y., Wang, C.-H., & Manga, M. (2004). Coseismic release of water from mountains: Evidence from the 1999 (Mw = 7.5) Chi-Chi, Taiwan, earthquake. *Geology*, 32(9), 769. <https://doi.org/10.1130/g20753.1>
- Wesnousky, S. G. (2008). Displacement and geometrical characteristics of earthquake surface ruptures: Issues and implications for seismic-hazard analysis and the process of earthquake rupture. *Bulletin of the Seismological Society of America*, 98(4), 1609–1632. <https://doi.org/10.1785/0120070111>
- Wessel, P., Smith, W. H. F., Scharroo, R., Luis, J., & Wobbe, F. (2013). Generic mapping tools: Improved version released. *Eos, Transactions American Geophysical Union*, 94(45), 409–410. <https://doi.org/10.1002/2013eo450001>
- Wiemer, S., & Wyss, M. (2000). Minimum magnitude of completeness in earthquake catalogs: Examples from Alaska, the western United States, and Japan. *Bulletin of the Seismological Society of America*, 90(4), 859–869. <https://doi.org/10.1785/0119990114>

- Wiemer, S., & Wyss, M. (2002). Mapping spatial variability of the frequency-magnitude distribution of earthquakes. In *Advances in Geophysics* (Vol. 45, pp. 259–V). Elsevier. [https://doi.org/10.1016/s0065-2687\(02\)80007-3](https://doi.org/10.1016/s0065-2687(02)80007-3)
- Wu, P., & Johnston, P. (2000). Can deglaciation trigger earthquakes in N. America? *Geophysical Research Letters*, 27(9), 1323–1326. <https://doi.org/10.1029/1999gl011070>
- Wu, Y. M., Chang, C. H., Zhao, L., Shyu, J. B. H., Chen, Y. G., Sieh, K., & Avouac, J. P. (2007). Seismic tomography of Taiwan: Improved constraints from a dense network of strong motion stations. *Journal of Geophysical Research*, 112. <https://doi.org/10.1029/2007jb004983>
- Wu, Y. M., Chang, C. H., Zhao, L., Teng, T. L., & Nakamura, M. (2008). A comprehensive relocation of earthquakes in Taiwan from 1991 to 2005. *Bulletin of the Seismological Society of America*, 98(3), 1471–1481. <https://doi.org/10.1785/0120070166>
- Wu, Y. M., Hsu, Y. J., Chang, C. H., Teng, L. S., & Nakamura, M. (2010). Temporal and spatial variation of stress field in Taiwan from 1991 to 2007: Insights from comprehensive first motion focal mechanism catalog. *Earth and Planetary Science Letters*, 298(3–4), 306–316. <https://doi.org/10.1016/j.epsl.2010.07.047>
- Wu, Y. M., Zhao, L., Chang, C. H., & Hsu, Y. J. (2008). Focal-mechanism determination in Taiwan by genetic algorithm. *Bulletin of the Seismological Society of America*, 98(2), 651–661. <https://doi.org/10.1785/0120070115>
- Yao, D. D., Walter, J. I., Meng, X. F., Hobbs, T. E., Peng, Z. G., Newman, A. V., et al. (2017). Detailed spatiotemporal evolution of microseismicity and repeating earthquakes following the 2012 M-w 7.6 Nicoya earthquake. *Journal of Geophysical Research: Solid Earth*, 122, 524–542. <https://doi.org/10.1002/2016jb013632>
- Yin, Y. P., Wang, F. W., & Sun, P. (2009). Landslide hazards triggered by the 2008 Wenchuan earthquake, Sichuan, China. *Landslides*, 6(2), 139–152. <https://doi.org/10.1007/s10346-009-0148-5>
- Zaliapin, I., & Ben-Zion, Y. (2021). Perspectives on clustering and declustering of earthquakes. *Seismological Research Letters*. <https://doi.org/10.1785/0220210127>
- Zhai, Q. S., Peng, Z. G., Chuang, L. Y., Wu, Y. M., Hsu, Y. J., & Wdowinski, S. (2021). A matched-filter-technique earthquake catalog in Taiwan from January 1, 2009, to July 31, 2010. Mendeley Data, V1. <https://doi.org/10.17632/cgys3svzrp.1>
- Zhang, Z.-X. (2016). Rock Fracture and Rock Strength. In *Rock Fracture and Blasting* (pp. 69–88). Elsevier. <https://doi.org/10.1016/b978-0-12-802688-5.00003-8>
- Zhu, L. J., Peng, Z. G., McClellan, J., Li, C. Y., Yao, D. D., Li, Z. F., & Fang, L. H. (2019). Deep learning for seismic phase detection and picking in the aftershock zone of 2008 M(w)7.9 Wenchuan Earthquake. *Physics of the Earth and Planetary Interiors*, 293, 106261. <https://doi.org/10.1016/j.pepi.2019.05.004>
- Zhuang, J., Ogata, Y., & Vere-Jones, D. (2002). Stochastic declustering of space-time earthquake occurrences. *Journal of the American Statistical Association*, 97(458), 369–380. <https://doi.org/10.1198/016214502760046925>
- Zhuang, J. C. (2006). Second-order residual analysis of spatiotemporal point processes and applications in model evaluation. *Journal of the Royal Statistical Society - Series B: Statistical Methodology*, 68(4), 635–653. <https://doi.org/10.1111/j.1467-9868.2006.00559.x>
- Zhuang, J. C., Chang, C. P., Ogata, Y., & Chen, Y. I. (2005). A study on the background and clustering seismicity in the Taiwan region by using point process models. *Journal of Geophysical Research*, 110(B5). <https://doi.org/10.1029/2004jb003157>
- Zhuang, J. C., Ogata, Y., & Vere-Jones, D. (2004). Analyzing earthquake clustering features by using stochastic reconstruction. *Journal of Geophysical Research*, 109(B5). <https://doi.org/10.1029/2003jb002879>